A REVERSE SHOCK IN GRB 181201A

Tanmoy Laskar[1], Hendrik van Eerten[1], Patricia Schady[1], C. G. Mundell[1], Kate D. Alexander[2*],
Rodolfo Barniol Duran[3], Edo Berger[4], J. Bolmer[5], Ryan Chornock[6], Deanne Coppejans[2], Wen-fai Fong[2],
Andreja Gomboc[7], Nuria Jordana[1], Shiho Kobayashi[8], Raffaella Margutti[2], Karl M. Menten[9], Re'em Sari[10],
Ryo Yamazaki[11], V. M. Lipunov[12,13], E. Gorbovskoy[13], V. G. Kornilov[12,13], N. Tyurina[13], D. Zimnukhov[13],
R. Podesta[14], H. Levato[15], D. A. H. Buckley[16], A. Tlatov[17], R. Rebolo[18], and M. Serra-Ricart[18]

[1]Department of Physics, University of Bath, Claverton Down, Bath, BA2 7AY, United Kingdom
[2] Center for Interdisciplinary Exploration and Research in Astrophysics (CIERA) and Department of Physics and Astronomy,
Northwestern University, Evanston, IL 60208, USA
[3]Department of Physics and Astronomy, California State University, Sacramento, 6000 J Street, Sacramento, CA 95819, USA
[4]Department of Astronomy, Harvard University, 60 Garden Street, Cambridge, MA 02138, USA
[5]Max-Planck-Institut für extraterrestrische Physik, Giessenbachstraße, 85748 Garching, Germany
[6]Astrophysical Institute, Department of Physics and Astronomy, 251B Clippinger Lab, Ohio University, Athens, OH 45701, USA
[7]Center for Astrophysics and Cosmology, University of Nova Gorica, Vipavska 13, 5000 Nova Gorica, Slovenia
[8]Astrophysics Research Institute, Liverpool John Moores University, IC2, Liverpool Science Park, 146 Brownlow Hill, Liverpool L3 5RF,
United Kingdom
[9]Max-Planck-Institut für Radioastronomie, Auf dem Hügel 69, 53121 Bonn, Germany
[10]Racah Institute of Physics, The Hebrew University, Jerusalem 91904, Israel
[11]Department of Physics and Mathematics, Aoyama-Gakuin University, Kanagawa 252-5258, Japan
[12]M. V. Lomonosov Moscow State University, Physics Department, Leninskie gory, GSP-1, Moscow, 119991, Russia
[13]M. V. Lomonosov Moscow State University, Sternberg Astronomical Institute, Universitetsky pr., 13, Moscow, 119234, Russia
[14]Observatorio Astronomico Felix Aguilar (OAFA), National University of San Juan, San Juan, Argentina
[15]Instituto de Ciencias Astronomicas, de la Tierra y del Espacio (ICATE), San Juan, Argentina
[16]South African Astrophysical Observatory, P.O. Box 9, 7935 Observatory, Cape Town, South Africa
[17]Kislovodsk Solar Station of the Main (Pulkovo) Observatory, RAS, P.O. Box 45, ul. Gagarina 100, Kislovodsk, 357700, Russia and
[18]Instituto de Astrofísica de Canarias (IAC), Calle Vía Láctea s/n, E-38200 La Laguna, Tenerife, Spain
Submitted to ApJ

ABSTRACT

We present comprehensive multiwavelength radio to X-ray observations of GRB 181201A spanning
from ≈ 150 s to ≈ 163 days after the burst, comprising the first joint ALMA-VLA-GMRT observations
of a gamma-ray burst (GRB) afterglow. The radio and mm-band data reveal a distinct signature at
≈ 3.9 days, which we interpret as reverse shock (RS) emission. Our observations present the first
time that a single radio-frequency spectral energy distribution can be decomposed directly into RS
and forward shock (FS) components. We perform detailed modeling of the full multiwavelength data
set, using Markov Chain Monte Carlo sampling to construct the joint posterior density function of
the underlying physical parameters describing the RS and FS synchrotron emission. We uncover and
account for all degeneracies in the model parameters. The joint RS-FS modeling reveals a weakly
magnetized ($\sigma \approx 3 \times 10^{-3}$), mildly relativistic RS, from which we derive an initial bulk Lorentz factor
of $\Gamma_0 \approx 103$ for the GRB jet. Our results support the hypothesis that low-density environments are
conducive to the observability of RS emission. We compare our observations to other events with
strong RS detections, and find a likely observational bias selecting for longer lasting, non-relativistic
reverse shocks. We present and begin to address new challenges in modeling posed by the present
generation of comprehensive, multi-frequency data sets.

Keywords: gamma-ray burst: general – gamma-ray burst: individual (GRB 181201A)

1. INTRODUCTION

Long-duration gamma-ray bursts, produced in the
core-collapse of massive stars, host the most ener-
getic, and most highly relativistic jets in the Universe
(Meszaros & Rees 1993; Rees & Meszaros 1994; Frail
et al. 1997; Woosley & Bloom 2006). However, the na-
ture of the central engine, as well as the mechanism by
which these jets are launched and collimated, remain
poorly understood (Mészáros 2006). Probing the nature
of the central engine, such as magnetars or an accreting
black hole, requires foremost determining the energetics
and composition of the GRB jets themselves (Metzger
et al. 2011; Lyutikov & Camilo Jaramillo 2017). Unfor-
tunately, the forward shock (FS) synchrotron 'afterglow'

emission, produced by interaction of the jet with the en-
vironment, is insensitive to the properties of GRB jets;
instead, the baryon content, initial bulk Lorentz factor,
and magnetization of the ejecta can be studied by cap-
turing emission from the reverse shock (RS), produced
in the jet during its rapid deceleration by the ambient
medium (Sari et al. 1998; Panaitescu & Kumar 2000;
Granot & Königl 2003; Granot & Taylor 2005; Zhang &
Kobayashi 2005).

Strong RSs are expected in ejecta where the mag-
netic field is dynamically unimportant and the ratio of
the magnetic energy density to the bulk kinetic energy,
$\sigma \lesssim 1$. On the other hand, highly magnetized out-
flows are expected to produce weak RS emission (Zhang
& Kobayashi 2005; McMahon et al. 2006; Lyutikov &
Camilo Jaramillo 2017). The expected signature of RS

radiation comprises a characteristic synchrotron spectrum superposed on the afterglow emission (Kobayashi 2000), resulting in an flash beginning in the optical and typically lasting a few tens of seconds to minutes, and which rapidly cascades to radio frequencies, where it typically lasts a few days (Akerlof et al. 1999; Sari & Piran 1999a; Nakar & Piran 2004).

Recent multi-wavelength observations have unequivocally isolated excess radio emission attributable to the RS, and a careful decomposition of the observed multi-frequency (radio to X-ray) spectral energy distribution (SED) at different epochs into FS and RS contributions has allowed the first inferences of the Lorentz factor and magnetization of GRB jets (Laskar et al. 2013; Perley et al. 2014; van der Horst et al. 2014; Laskar et al. 2016; Alexander et al. 2017; Laskar et al. 2018b,c). These works have usually provided point estimates on the RS parameters with no uncertainty estimates, owing to limitations of the modeling process.

Here, we present multi-wavelength observations of GRB 181201A spanning from ≈ 150 s to ≈ 163 days after the burst at 35 frequencies from 6×10^8 Hz to 3×10^{17} Hz, including the first joint Giant Meterwave Radio Telescope (GMRT), Karl G. Jansky Very Large Array (VLA), and Atacama Large Millimeter/submillimeter Array (ALMA) data set (Section 2). Our radio and mm-band observations reveal an RS spectral peak superposed on the FS emission, which we are able to decompose into RS and FS components in a single radio SED for the first time (Section 3), while using the optical and X-ray observations to constrain the nature of the circum-burst environment. We fit the entire multiwavelength dataset simultaneously to derive the properties of the RS and FS emission, and demonstrate that the two components are consistent with emission from a double shock system (Section 4). We use this decomposition to derive the initial Lorentz factor and magnetization of the ejecta using full statistical modeling. We conclude with a detailed discussion of the results, placed in context of other GRBs with multi-wavelength RS detections (Section 5). Unless otherwise stated, all uncertainties are reported at the 1σ level, all magnitudes are in the AB system and not corrected for Galactic extinction. We employ ΛCDM cosmological parameters of $\Omega_m = 0.31$, $\Omega_\Lambda = 0.69$, and $H_0 = 68 \, \mathrm{km \, s^{-1} \, Mpc^{-1}}$ throughout.

2. OBSERVATIONS AND DATA ANALYSIS

GRB 181201A was discovered by the IBIS and ISGRI instruments on-board the *INTEGRAL* satellite on 2018 December 1 at 02:38 UT (Mereghetti et al. 2018). The burst, which lasted ≈ 180 s, saturated the telemetry, and hence only a lower limit to its γ-ray flux is available from *INTEGRAL*. The GRB was also detected by the *Fermi* Large Area Telescope (LAT) beginning at 02:38:00 UT (Arimoto et al. 2018), by *Konus*-Wind at 02:39:52.36 UT with a burst duration of ≈ 172 s (Svinkin et al. 2018), and by *Astrosat* with a duration of $T_{90} \approx 19.2$ s (Khanam et al. 2018). We take the *Fermi* and *INTEGRAL* time as T_0 for this burst, and reference all times hereafter to this T_0. The time-averaged *Konus*-Wind spectrum in the 20 keV - 10 MeV energy range can be fit with a Band model, with low energy photon index, $\alpha_\gamma = -1.25 \pm 0.05$, high energy photon index $\beta = -2.73^{+0.11}_{-0.12}$, peak energy,

Table 1
Swift UVOT Observations of GRB 181201A

Mid-time, Δt (d)	UVOT band	Flux density (mJy)	Uncertainty (mJy)	Detection? (1=Yes)
0.176	*uw2*	6.19×10^{-1}	2.92×10^{-2}	1
0.246	*uw2*	4.61×10^{-1}	2.17×10^{-2}	1
0.302	*uw2*	3.31×10^{-1}	1.88×10^{-2}	1
$\cdots$	$\cdots$	$\cdots$		

Note. — This is a sample of the full table available on-line.

$E_{\gamma,\mathrm{peak}} = (152 \pm 6)$ keV, and a fluence of $(1.99 \pm 0.06) \times 10^{-4} \, \mathrm{erg \, cm^{-2}}$ (Svinkin et al. 2018).

The optical afterglow was discovered in MASTER (Lipunov et al. 2010) Global Robotic Net observations (Podesta et al. 2018) 10 s after the *INTEGRAL* alert and later by the *Swift* UV/optical telescope (UVOT; Roming et al. 2005) (Siegel & Cannizzo 2018). Spectroscopic observations with the Very Large Telescope at the European Southern Observatory yielded a redshift of $z = 0.450$ based on identification of the Mg II doublet (Izzo et al. 2018). At this redshift, the *Konus*-Wind spectrum implies an isotropic-equivalent γ-ray energy of $E_{\gamma,\mathrm{iso}} = (1.20 \pm 0.04) \times 10^{53}$ erg, This value is consistent with the GRB E_{peak}-$E_{\gamma,\mathrm{iso}}$ relation (Amati 2006), suggesting that the prompt γ-ray emission in GRB 181201A is typical among the GRB population.

2.1. *X-ray: Swift/XRT*

The *Swift* X-ray Telescope (XRT, Burrows et al. 2005) began observing GRB 181201A 0.16 days after the burst, and detected a fading X-ray afterglow at RA = $21^\mathrm{h}17^\mathrm{m}11^\mathrm{s}.20$, Dec = -12° 37′ 50.9″ (J2000), with an uncertainty radius of 1.4″ (90% containment)[2]. XRT continued observing the afterglow for 20 d in photon counting mode. The GRB entered a Sun constraint for *Swift* at ≈ 21 days after the burst and was dropped from the *Swift* schedule. We obtained 4.4 ks of *Swift* ToO observations on 2019 April 7 (≈ 127 days), when it was visible again. The X-ray afterglow was weakly detected. The data were automatically calibrated using the XRT pipeline and incorporated into the on-line light curve. We use a photon index of $\Gamma_\mathrm{X} \approx 1.77$ and an unabsorbed counts-to-flux conversion rate from the *Swift* website of $4.75 \times 10^{-11} \, \mathrm{erg \, cm^{-2} \, ct^{-1}}$ to convert the 0.3–10 keV count rate light curve[3] to flux density at 1 keV for subsequent analysis.

2.2. *UV, optical, and near-IR*

We derived aperture photometry from pipeline processed UVOT images downloaded from the *Swift* data center[4] with the UVOTPRODUCT (v2.4) software. We used a circular source extraction region with a 3.5″ radius, followed by an aperture correction based on the standard 5″ aperture for UVOT photometry (Poole et al. 2008). We present our UVOT measurements in Table 1.

[2] http://www.swift.ac.uk/xrt_positions/00020848/
[3] Obtained from the *Swift* website at http://www.swift.ac.uk/xrt_curves/00020848 and re-binned to a minimum signal-to-noise ratio per bin of 8.
[4] http://www.swift.ac.uk/swift_portal

Table 2
Optical and Near-IR Observations of GRB 181201A

Δt (d)	Observatory	Instrument	Filter	Frequency (Hz)	Flux density (mJy)	Uncertainty (mJy)	Detection? 1=Yes	Reference
1.81×10^{-3}	MASTER-OAFA	MASTER	CR	4.67×10^{14}	1.25×10^{1}	1.27×10^{-1}	1	This work
2.42×10^{-3}	MASTER-OAFA	MASTER	CR	4.67×10^{14}	2.85×10^{1}	1.58×10^{-1}	1	This work
3.46×10^{-1}	iTelescope	T31	R	4.67×10^{14}	6.52×10^{-1}	1.83×10^{-2}	1	Kong (2018)
...	...	...	...	...	...	...	...	...

Note. — The data have not been corrected for Galactic extinction. This is a sample of the full table available on-line.

Four MASTER-net observatories (MASTER-Kislovodsk, MASTER-IAC, MASTER-SAAO, and MASTER-OAFA) participated in rapid-response and follow-up observations of GRB181201A, beginning with 10 s exposures at 02:40:30 UT on 2019 December 1, $\approx$ 150 s after the burst and 10 s after the *INTEGRAL* alert in $BVRI$ and Clear bands[5] (Podesta et al. 2018). The MASTER auto-detection system (Lipunov et al. 2010, 2019) discovered a bright optical afterglow at RA = $21^{\mathrm{h}}17^{\mathrm{m}}11\overset{\mathrm{s}}{.}20$, Dec = -12° 37′ 51.4″ (J2000) with unfiltered magnitude $\approx$ 13.2 mag (Vega). MASTER follow-up observations continued until $\approx$ 3 days after the burst. We carried out astrometry and aperture photometry (using a $\approx$ 2.5″ aperture radius) for observations taken at each telescope separately, calibrated to 6 nearby SDSS reference stars. We verified our photometry by measuring the brightness of comparison stars with similar brightness as the afterglow, and incorporated the derived systematic calibration uncertainty in to the photometric uncertainty (Troja et al. 2017; Lipunov et al. 2019).

We observed the afterglow of GRB 181201A with the Gamma-Ray Burst Optical/Near-Infrared Detector (GROND) on the MPI/ESO 2.2m telescope in La Silla in Chile beginning 0.91 days after the burst in $g'r'i'z'JHK$ filters. We calibrated the data with tools and methods standard for GROND observations, and detailed in Krühler et al. (2008). We performed aperture photometry calibrated against PanSTARRS field stars in the $g'r'i'z'$ filters, and against the 2MASS catalog in JHK.

We observed the afterglow with the Ohio State Multi-Object Spectrograph (OSMOS; Martini et al. 2011) on the 2.4 m Hiltner telescope at MDM Observatory on 2018 December 04, with 120 s exposures each in $BVRI$ bands. We obtained two later epochs of imaging using the Templeton detector on the 1.3m McGraw-Hill telescope on the nights of 2018 December 9 and 10, obtaining 4×300 s each in r' and i' bands. Observations on December 10 were taken at a high airmass of 1.91 and under poor seeing. We performed aperture photometry with a 2″ aperture on the Hiltner and McGraw-Hill images, referenced to SDSS.

We obtained Liverpool Telescope (LT; Steele et al. 2004) imaging with the infrared/optical camera (IO:O) at $\approx$ 2.7 days, comprising 3×120 s exposures in $g'r'i'$ bands. We performed aperture photometry using the Astropy Photutils package (Bradley et al. 2016) calibrated to SDSS. We also collected all optical photometry for this event published in GCN circulars. We present our

---

[5] MASTER Clear band (CR) magnitudes are best described by the ratio, $CR = 0.8R + 0.2B$.

Table 3
Radio and millimeter observations of GRB 181201A

Telescope	Frequency (GHz)	Time (days)	Flux density (mJy)	Uncertainty (μJy)
ALMA	97.5	0.885	3.41	23
ALMA	96.4	1.92	1.99	25
VLA	2.73	2.93	0.478	70
...	...	...	...	...

Note. — This is a sample of the full table available on-line.

combined optical and NIR data set in Table 2.

2.3. *Millimeter: ALMA*

We obtained 5 epochs of ALMA Band 3 (3 mm) observations of GRB 181201A spanning 0.88 days to 29.8 days after the burst through program 2018.1.01454.T (PI: Laskar). The observations utilized two 4 GHz-wide basebands centered at 91.5 and 103.5 GHz, respectively, in the first epoch, and at 90.4 and 102.4 GHz in subsequent epochs. One of J2258-2758, J2148+0657, and J2000-1748 was used for bandpass and flux density calibration, while J2131-1207 was used for complex gain calibration in all epochs. We analyzed the data using the Common Astronomy Software Application (McMullin et al. 2007, CASA) and the afterglow was well-detected in all epochs. We performed one round of phase-only self-calibration in the first two epochs, where the deconvolution residuals indicated the presence of phase errors. We list the results of our ALMA observations in Table 3.

2.4. *Centimeter: VLA*

We observed the afterglow using the VLA starting 2.9 d after the burst through programs 18A-088 and 18B-407 (PI: Laskar). We detected and tracked the flux density of the afterglow from 1.2 GHz to 37 GHz over multiple epochs until $\approx$ 164 d after the burst. We used 3C48 as the flux and bandpass calibrator and J2131-1207 as complex gain calibrator. Where phase errors appeared to be present after deconvolution, we performed phase-only self-calibration in epochs with sufficient signal-to-noise. The effect of self-calibration impacted the measured flux density by $\lesssim$ 15% and only at the highest frequencies ($\gtrsim$ 15 GHz). We carried out data reduction using CASA, and list the results of our VLA observations in Table 3.

2.5. *Meter: uGMRT*

We observed the afterglow using the upgraded Giant Meterwave Radio Telescope (uGMRT) through program 35_065 (PI: Laskar) starting 12.5 d and 13.5 d after the burst in Bands 4 (center frequency 550 MHz) and 5

(center frequency 1450 MHz), respectively. The observations utilized the full 400 MHz bandwidth of the uGMRT Wide-band Backend (GWB) system. We used 3C48 for bandpass and flux density calibration, and J2131-1207 for complex gain calibration. We carried out data reduction using CASA, and list the results of our uGMRT observations in Table 3.

3. BASIC CONSIDERATIONS

We now interpret the X-ray to radio afterglow observations in the context of synchrotron emission arising from relativistic shocks. The observed spectral energy distribution (SED) of each synchrotron component is described by three break frequencies (the self-absorption frequency, ν_a, the characteristic frequency, ν_m, and the cooling frequency, ν_c), and the flux density normalization, $F_{\nu,m}$. The evolution of these quantities with time depends upon the radial density profile of the circumburst medium, $\rho \propto R^{-k}$, for which we consider two standard possibilities: a constant density ($k = 0$; ISM) model (Sari et al. 1998) and a wind-like ($k = 2$) environment (Chevalier & Li 2000).

3.1. Radio/mm: presence of additional component

One of the most striking features of GRB 181201A revealed by our VLA and ALMA observations is a spectral bump in the cm to mm-band SED at 3.9 days (Fig. 1). The feature spans 3–24 GHz, and can be fit with a smoothly broken power law, with low-frequency index[6], $\beta_1 = 1.43\pm0.23$, high-frequency index, $\beta_2 = -0.35\pm0.03$, break frequency, $\nu_{peak} = 5.5 \pm 0.4$ GHz, and peak flux density, $F_{\nu,peak} = 1.48 \pm 0.06$ mJy. The steeply rising spectrum below the spectral peak suggests the underlying emission is self-absorbed[7]. Fitting the VLA cm-band data above 24 GHz and the ALMA observations at the same epoch with a single power law model yields $\beta_{24-\mathrm{ALMA}} = 0.09 \pm 0.02$.

The radio and millimeter SED at 3.9 days clearly exhibits two distinct components. The simplest explanation for multiple components in the radio is to attribute one to a RS and the other to a FS. Since the RS emission is expected to peak at lower frequencies than the FS and the RS spectrum is expected to cut off steeply above the RS cooling frequency (Kobayashi 2000), the lower-peaking component is more naturally associated with RS emission.

The ALMA mm-band light curve can be fit with a single power law, with decay rate $\alpha_{\mathrm{ALMA}} = -0.71 \pm 0.01$ (Fig. 2). From the radio SED at 3.9 days, we know that $\nu_{m,f} > \nu_{\mathrm{ALMA}}$ at this time. In this spectral regime, the expected rise rate for FS emission is $t^{1/2}$ in the ISM environment and t^0 in the wind environment, both of which are incompatible with the observed mm-band light curve. Thus, the mm-band light curve at < 4 days originates from a separate component. The shallowest decline rate for an RS light curve at $\nu \gtrsim \nu_{m,r}$ is $\alpha \approx -2.1$ for a relativistic RS and $\alpha - 1.5$ for a non-relativistic RS, in each case corresponding to a wind environment with $p \approx 2$. Both of these are steeper than the observed mm-band

---

[6] We use the convention $F_\nu \propto t^\alpha \nu^\beta$ throughout.

[7] The deviation of this low-frequency power law from the expected value of $\beta \approx 2$ arises from a contribution from an underlying $\nu^{1/3}$ power law extending down from the mm band (Section 4).
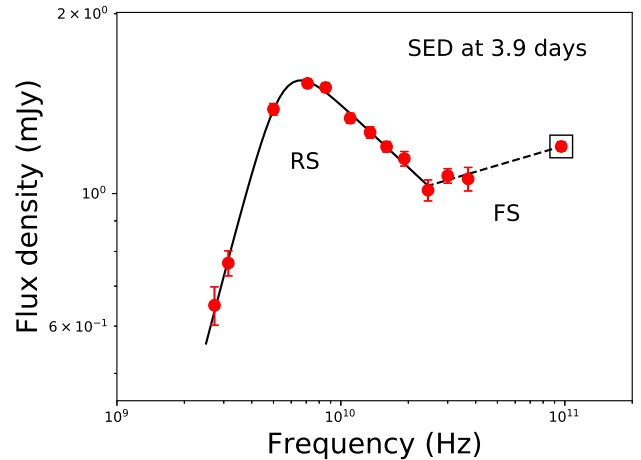

Figure 1. Radio and mm-band SED of GRB 181201A at 3.9 days post-burst from our VLA and ALMA programs, with a broken power law fit at 3–24 GHz (solid) and a single power law at high frequencies (dashed). The cm-band data spanning 3–24 GHz exhibit a self-absorbed spectral peak, which we attribute to emission from a reverse shock. The VLA observations above 24 GHz and the the ALMA data (highlighted by a black box) constrain the high-frequency rising spectrum with index $\beta = 0.09 \pm 0.02$, and form a distinct emission component, which we associate with underlying forward shock emission (Section 3.1).

light curve. However, the sum of the contributions from the two emission components (RS and FS) may yield the observed shallower decay. We investigate this further in Section 5.2.

For the remainder of this article, we associate the low- and high-frequency components with emission from the RS and the FS, respectively, and consider other scenarios in Section 5.5. In this framework, our observations of GRB 181201A provide the first instance where a single radio SED can be instantaneously and cleanly decomposed into RS and FS components, with the RS dominating at the lower frequency bands, and the underlying FS emission clearly visible as an optically thin, rising spectrum at higher frequencies. We note that a more detailed characterization of these components, including the determination of the precise locations of their spectral break frequencies, requires a multi-band model fit, which we undertake in Section 4.

3.2. Circum-burst density profile

The identification of the FS component now allows us to constrain the circum-burst density profile. We note that there is no evidence for a jet break until ≈ 21 days, as the X-ray light curve declines as a single power law from ≈ 0.15 days to ≈ 21 days ($\alpha_X = -1.22 \pm 0.01$; Fig. 3). The rising radio spectrum to ≈ 90 GHz at 3.9 days indicates that $\nu_{m,f} \gtrsim 90$ GHz at this time. The relatively shallow spectral index of $\beta \approx 0.1$ compared to the expected index of $\beta = 1/3$ may result from the smoothness and potential proximity of the $\nu_{m,f}$ break (Granot & Sari 2002).

Since $\nu_{m,f} \gtrsim 90$ GHz at 3.9 days, the FS peak flux density, $F_{\nu,m,f} \gtrsim F_{3\,\mathrm{mm}}(3.9\text{ days}) \approx 1.2$ mJy. In the ISM environment, this peak flux density, F_p, remains fixed and must appear at a lower cm-band frequency, ν_{cm}, at
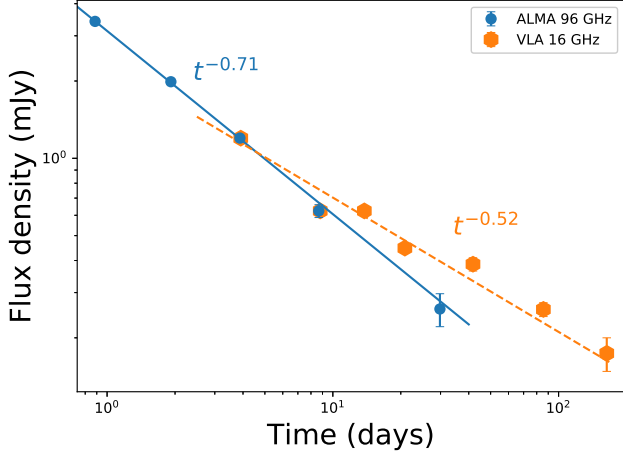
Figure 2. ALMA Band 3 (3 mm) light curve of GRB 181201A from ≈ 0.9 days to 30 days after the burst (blue circles) with a power law model fit (blue line; $\alpha = -0.71 \pm 0.01$), along with VLA 16 GHz light curve (orange) and corresponding power law fit for comparison. The steep light curve decay indicates a wind-like pre-explosion environment (Section 3.2).
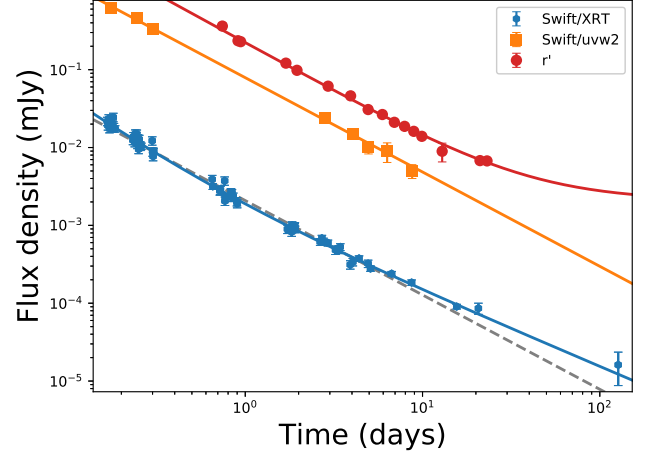

Figure 3. Optical r'-band, *Swift*/UVOT *uvw2*-band, and *Swift*/XRT 1 keV light curves of GRB 181201A, together with a power-law-plus-constant fit (red; r'-band), power-law fit at *uvw2*-band, and power-law (grey, dashed) and broken power law fit (blue; X-ray). The excess emission in r'-band at $\gtrsim 10$ days may indicate contamination from the underlying host galaxy.

a later time given by,

$$t_{\rm p} = \left(\frac{\nu_{\rm ALMA}}{\nu_{\rm cm}} \right)^{2/3} \left(\frac{F_{\rm p}}{F_{\rm ALMA}} \right)^2 . \qquad (1)$$

This implies a flux density of $F_{\rm p} \gtrsim 1.2$ mJy at $t_{\rm p} \gtrsim 13.2$ days at 16 GHz, which is a factor of 2 brighter than the observed 16 GHz light curve at the corresponding time. Indeed, all cm-band light curves are inconsistent with this extrapolation, and thus inconsistent with an ISM-like environment.

We now show that the optical to X-ray data are also inconsistent with an ISM environment, and indicate a wind-like circum-burst medium. The GROND SED at 0.91 days corrected for Galactic extinction of $A_{\rm V} = 0.17$ mag (Schlafly & Finkbeiner 2011) can be fit with a single power law, with index $\beta_{\rm opt} = -0.49 \pm 0.04$ (Fig. 4). On the other hand, the spectral index between the GROND K-band and the X-rays is steeper, $\beta_{\rm NIR,X} = -0.75 \pm 0.02$, indicating that a spectral break lies between the optical/NIR and X-rays. The most natural explanation for these observations is $\nu_{\rm m,f} < \nu_{\rm opt} < \nu_{\rm c,f} < \nu_{\rm X}$. Fitting the optical and X-ray SED at 0.9 days, 2.9 days, and 4.9 days with broken power law models[8] fixing the low frequency index to $\beta_{\rm opt} = -0.5$ and the high frequency index to $\beta_{\rm X} = -1.0$, we find a break frequency, $\nu_{\rm b} = (5.7 \pm 1.5) \times 10^{15}$ Hz, $(8.1 \pm 2.0) \times 10^{15}$ Hz, and $(9.1 \pm 3.3) \times 10^{15}$ Hz, respectively (Fig. 4). The rising break frequency is roughly consistent with the evolution of $\nu_{\rm c,f} \propto t^{1/2}$ in a wind-like environment. We caution that the inferred location of the break is only indicative, as it is degenerate with the spectral slopes and break smoothness.

For $\nu_{\rm m,f} < \nu_{\rm opt} < \nu_{\rm c}$, we expect a spectral index of $\beta = (1-p)/2$. Combined with the observed GROND SED at 0.9 days, this implies $p \approx 2$, which yields a light

curve decay rate of $\alpha_{\rm opt} \approx -1.25$ for the wind environment and $\alpha_{\rm opt} \approx -0.75$ for the ISM environment. The observed decay rate in the *Swift*/UVOT *uvw2*-band and in ground-based optical r'-band observations at ≈ 0.2–8.7 days is $\alpha_{\rm UV} = -1.21 \pm 0.02$, consistent with the wind case and inconsistent with an ISM environment (Fig. 3).

Above $\nu_{\rm c,f}$, we expect a decay rate of $\alpha = (2 - 3p)/4 \approx -1$. A power law fit to the X-ray light curve yields a decay rate of $\alpha_{\rm X} = -1.212 \pm 0.013$; however, the light curve after ≈ 6 days is consistently above the single power law fit. Adding a temporal break at $t_{\rm b} \approx 0.4$ days yields a better fit with $\alpha_{X,1} = -1.7 \pm 0.1$ and $\alpha_{X,2} = -0.96 \pm 0.02$. The steep early decay may imply that the cooling break is not far below the X-ray band, and we verify this with our full multi-wavelength model in Section 4.1. On the other hand, the late-time excess is unusual, and we discuss this further in Section 5.3.

The measured X-ray photon index of $\Gamma_{\rm X} = 1.77 \pm 0.06$ implies $\beta_{\rm X} = -0.77 \pm 0.06$, which is not consistent with $\beta = -p/2 \approx -1$ expected for $p \approx 2$. We note that the Klein-Nishina (KN) correction may yield a spectral index of $\beta = -3(p-1)/4 \approx -0.75$ in some regimes (Nakar et al. 2009), and it is possible that this may impact the X-ray spectrum but not the light curve[9]. We defer a detailed discussion of the KN corrections to future work.

To summarize, the radio SED at 3.9 days and the mm-band light curve indicate the presence of a separate emission component than that responsible for the X-ray and optical emission. We interpret this low-frequency component as RS emission. Furthermore, we have described several observations that favor a wind-like circum-burst environment: (i) the high mm-band flux density at 4 days that does not appear in the lower frequency radio light

---

[8] $F_{\nu} = F_{\rm b} \left[\frac{1}{2} \left(\frac{\nu}{\nu_{\rm b}} \right)^{-y\beta_1} + \frac{1}{2} \left(\frac{\nu}{\nu_{\rm b}} \right)^{-y\beta_2} \right]^{-1/y}$. We fix $y = 3$ in this fit to emulate a moderately smooth break.

[9] When $p \approx 2$, the effect of KN corrections on the evolution of $\nu_{\rm c}$ with time, and hence on the light curve above $\nu_{\rm c}$, is small. However, the spectral corrections remain, and in particular, we may have $\nu_{\rm c} < \widehat{\nu}_{\rm c} < \nu_{\rm X}$, which would result in a spectral index of $\beta \approx -0.75$ (Nakar et al. 2009). Here $\widehat{\nu}_{\rm c}/\nu_{\rm c} = (\widehat{\gamma}_{\rm c}/\gamma_{\rm c})^2$, $\widehat{\gamma}_{\rm c} = \gamma_{\rm self}^3/\gamma_{\rm c}^2$, $\gamma_{\rm self} = (B_{\rm QED}/B)^{1/3}$, B is the post-shock magnetic field, and $B_{\rm QED}$ is the quantum critical field.
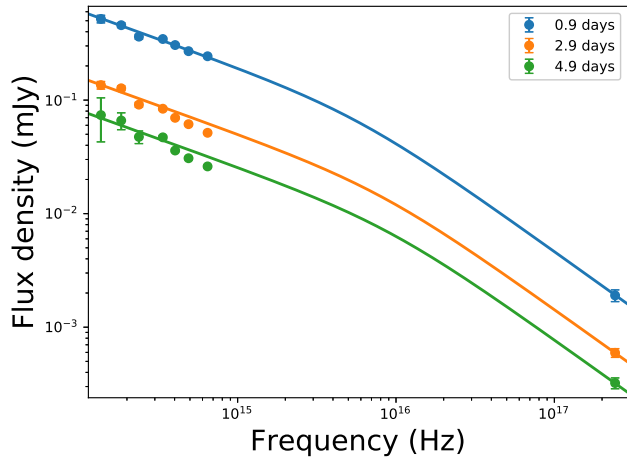
Figure 4. UV to X-ray SEDs at 0.9, 2.9, and 4.9 days, together with broken power law model fits (lines). The spectral break suggests $\nu_{\rm opt} < \nu_{\rm c,f} < \nu_X$ at this time (Section 3.2.

curve, (ii) a slowly rising break between the optical and X-rays, and (iii) the optical light curve, which is consistent with $\nu_{\rm m,f} < \nu_{\rm opt} < \nu_c$ in a wind environment. We therefore focus on the wind environment in the remainder of this article.

3.3. *Afterglow onset*

The first two MASTER observations at 156 and 209 s after the burst (156 s and 209 s, respectively) reveal a rapid brightening, $\alpha \approx 2.8$. Such brightenings have only been seen in a few other optical afterglows (Molinari et al. 2007; Melandri et al. 2010; Liang et al. 2010), and have been interpreted as onset of the afterglow, where the increase in flux density corresponds to an on-going transfer of energy from the ejecta to the forward shock, ultimately resulting in the deceleration of the ejecta (Rees & Meszaros 1992; Meszaros & Rees 1993; Sari & Piran 1999b; Kobayashi et al. 1999; Kobayashi & Zhang 2007). Unfortunately, our data do not capture the time of the peak in the optical bands. As the FS is not fully set up during this onset period, we do not include these points in our multiwavelength modeling (Section 4). We discuss these data further in Section 5.1.

4. MULTI-WAVELENGTH MODELING
4.1. *Markov Chain Monte Carlo Analysis*

Guided by the basic considerations discussed above, we fit all available X-ray to radio observations with a model comprising an FS and RS produced by a relativistic jet propagating in a wind-like circum-burst environment. The free parameters for the FS model are p, $E_{\rm K,iso,52}$, A_*, ϵ_e, ϵ_B, and the extinction, A_V. Given the relatively shallow decline rate of the mm-band light curve ($\alpha \approx -0.72$) corresponding to the RS component, we focus on the non-relativistic RS model, which allows for shallower light curve decay than a relativistic RS. The free parameters for the RS model[10] are the break frequencies $\nu_{\rm a,r}$, $\nu_{\rm m,r}$, $\nu_{\rm c,r}$ and the RS peak flux, $F_{\nu,\rm m,r}$ all at a

---

[10] We opt to fit for the observable quantities rather than the derived quantities of Γ_0, $t_{\rm dec}$, and R_B for the RS, as these observables uniquely specify the RS spectrum independent of the FS parameters during the fitting process.

Table 4
FS and RS Model Parameters

Parameter	Best fit	MCMC[a]
Forward Shock		
p	2.11	2.11 ± 0.01
$\log \epsilon_e$	-0.43	$-0.39^{+0.12}_{-0.17}$
$\log \epsilon_B$	-2.01	$-2.20^{+0.42}_{-0.78}$
$\log A_*$	-1.72	$-1.66^{+0.23}_{-0.13}$
$\log(E_{\rm K,iso}/{\rm erg})$	53.3	$53.41^{+0.13}_{-0.16}$
$\log(A_V/{\rm mag})$	-1.83	$-1.84^{+0.14}_{-0.18}$
$\log \nu_{\rm a,f}$ (Hz)	$7.74^{\rm b}$	...
$\log \nu_{\rm m,f}$ (Hz)	12.7	...
$\log \nu_{\rm c,f}$ (Hz)	16.4	...
$\log F_{\nu,\rm m,f}$ (mJy)	0.62	...
Reverse Shock		
$\log(\nu_{\rm a,r}/{\rm Hz})$	12.1	12.11 ± 0.06
$\log(\nu_{\rm m,r}/{\rm Hz})$	8.6	$8.64^{+1.01}_{-0.45}$
$\log(\nu_{\rm c,r}/{\rm Hz})$	14.7	$14.65^{+0.25}_{-0.22}$
$\log(F_{\nu,\rm m,r}/{\rm mJy})$	5.2	$5.16^{+0.26}_{-0.56}$
g	2.72	$2.74^{+0.38}_{-0.31}$

Note. — Frequencies and flux densities are calculated at 1 day (FS) and 10^{-2} days (RS).
[a] Summary statistics from the marginalized posterior density distributions, with median and $\pm 34.1\%$ quantiles (corresponding to $\pm 1\sigma$ for Gaussian distributions; Fig. 7).
[b] This frequency is not directly constrained by the data.

reference time, $t_{\rm ref} \equiv 0.01$ days selected to be $\approx$ few $\times T_{90}$ (and hence comparable to $t_{\rm dec}$). Additionally, we allow the parameter g, corresponding to the evolution of the RS Lorentz factor with radius after the deceleration time ($\Gamma \propto R^{-g}$) to vary (Mészáros & Rees 1999; Kobayashi & Sari 2000). Finally, we allow for a constant contribution to the light curves from an underlying host galaxy in bands where late-time flattening is evident (optical *griz* bands and the cm-bands from 2.7 to 24.5 GHz). All free parameters, including RS and FS components and the underlying host galaxy contamination, are fit simultaneously. Further details of the modeling procedure, including the likelihood function employed, are described elsewhere (Laskar et al. 2013, 2014, 2016).

We performed a Markov Chain Monte Carlo (MCMC) exploration of the multi-dimensional parameter space using `emcee` (Foreman-Mackey et al. 2013). We ran 512 walkers for 10k steps and discarded a few ($\lesssim 0.15\%$) initial non-converged steps with low log likelihood as burn-in. Our highest likelihood model with $p \approx 2.1$, $\epsilon_e \approx 0.37$ $\epsilon_B \approx 9.6 \times 10^{-3}$, $E_{\rm K,iso} \approx 2.2 \times 10^{53}$ erg, $A_* \approx 1.9 \times 10^{-2}$, and negligible extinction, $A_V \lesssim 0.02$ mag, together with an RS model with $g \approx 2.7$, $\nu_{\rm a,r} \approx 4.2$ GHz, $\nu_{\rm c,r} \approx$ 90 GHz, and $F_{\nu,\rm a,r} \approx 0.6$ mJy at 3.9 days fits the X-ray to radio light curves and radio SEDs well (Figs. 5 and 6). The peak in the cm-band spectrum at 3.9 days corresponds to $\nu_{\rm a,r}$. The sum of the RS self-absorbed spectrum and the FS optically thin $\nu^{1/3}$ spectrum below $F_{\nu,\rm a,r}$ (Fig. 6) explains the intermediate $\beta \approx 1.4$ spectral index below the cm-band peak (Section 3.1). We present a selection of SEDs spanning radio to X-rays, and all light curves together in a single figure in the appendix
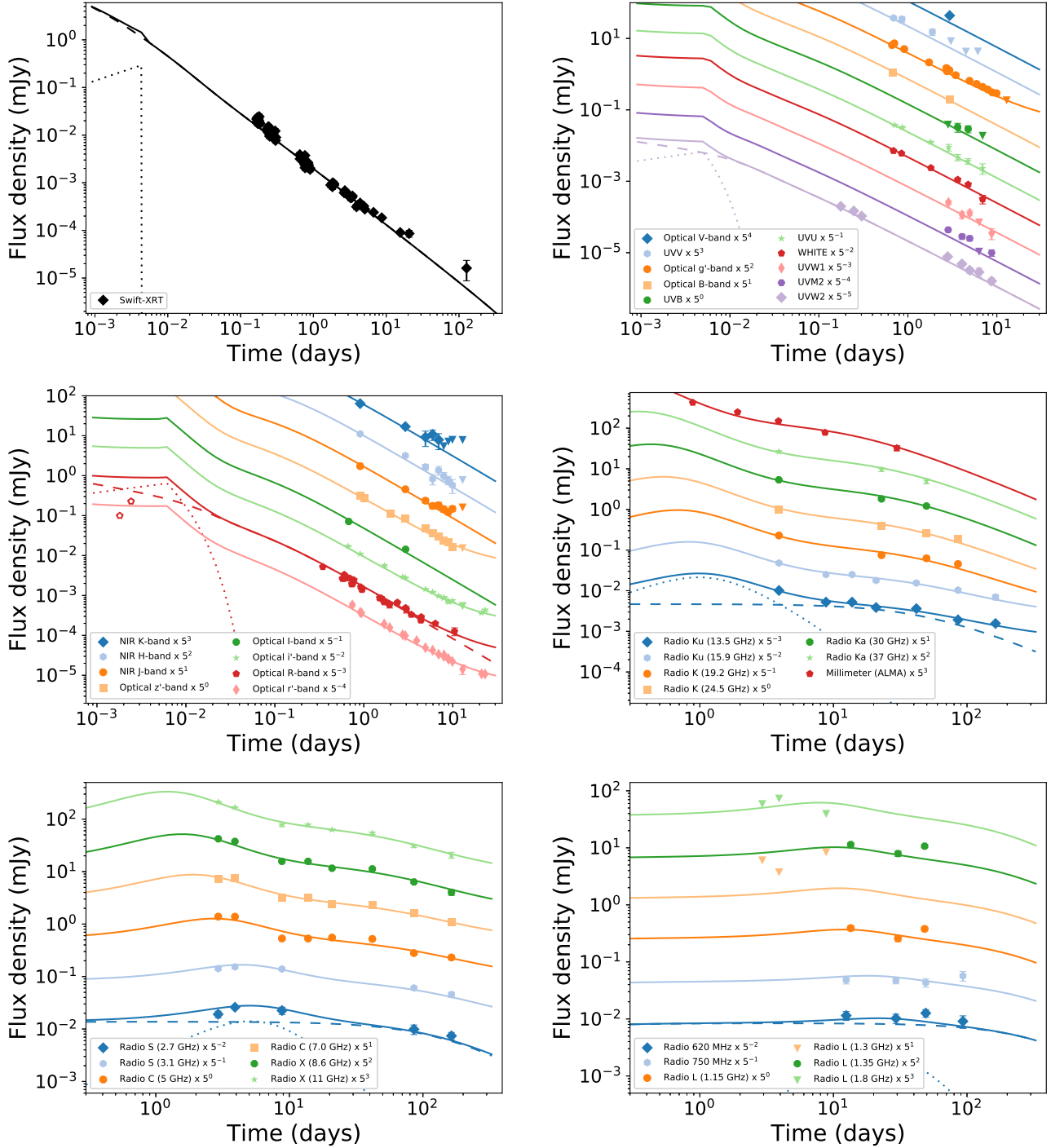
Figure 5. X-ray (top left), UV/optical (top right), optical/NIR (center left), and radio (center right and bottom) light curves of GRB 181201A, together with a full FS+RS model (solid lines). Data represented by open symbols are not included in the model fit. We show a decomposition of the X-ray, *Swift/w*2-band, optical *R*-band, 13.5 GHz, 2.7 GHz, and 620 MHz light curves into FS (dashed) and RS (dotted) components. Light curves exhibiting a late-time flattening incorporate a contribution from the underlying host galaxy (Section 4.1). The combined model explains the overall behavior of the light curves at all 36 observing frequencies. See Fig. 13 in the appendix for a combined plot showing all lightcurves together.

LASKAR ET AL.
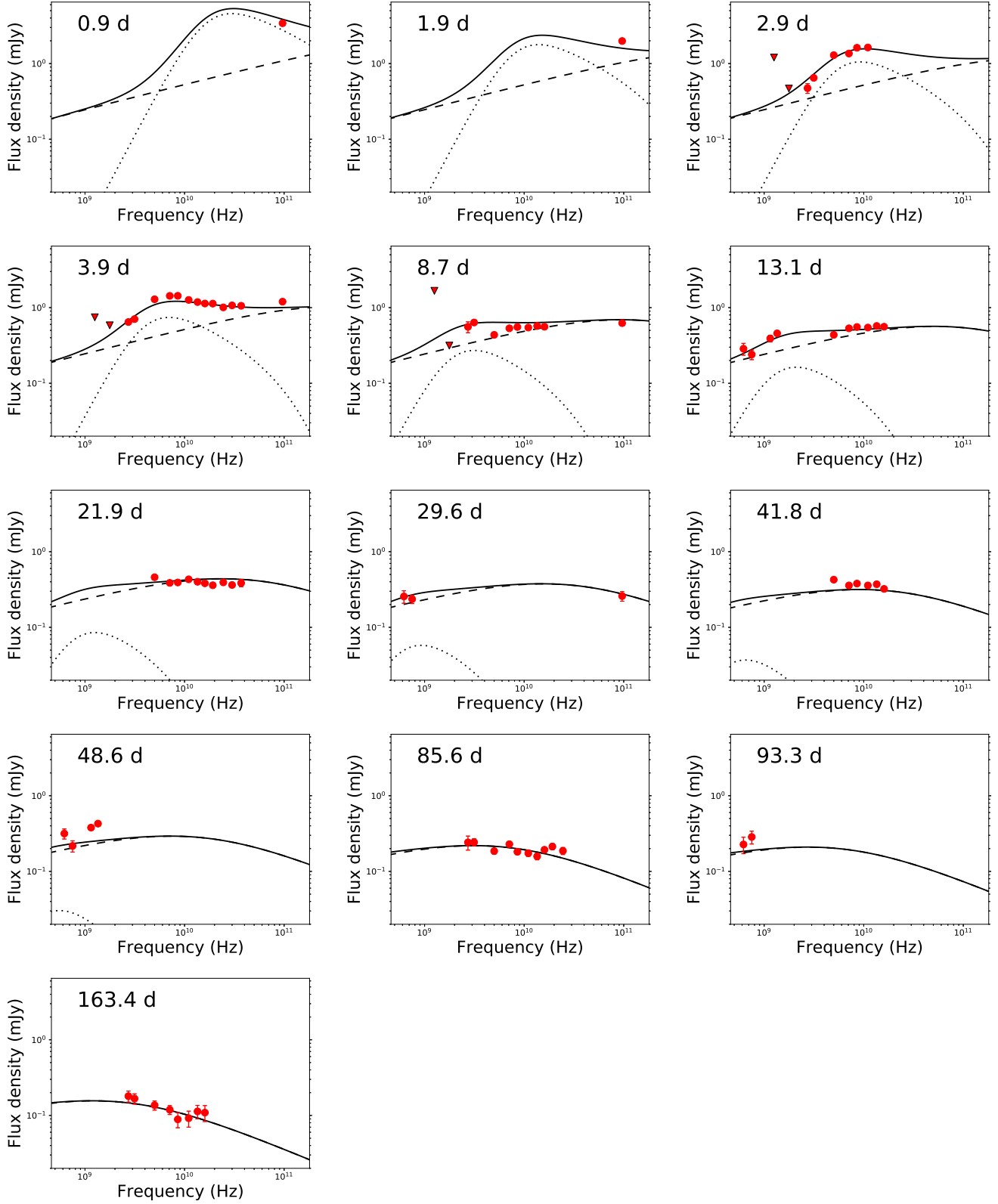
Figure 6. VLA cm-band and ALMA mm-band spectral energy distributions of GRB 181201A at multiple epochs starting at 0.9 days, together with the same FS+RS wind model as in Figure 5 (solid), decomposed into FS (dashed) and RS (dotted) contributions. The contribution of the host galaxy (included in the modeling) has been subtracted from the measured flux density at each frequency. See Fig. 12 in the appendix for a plot showing these SEDs together with optical and X-ray observations.
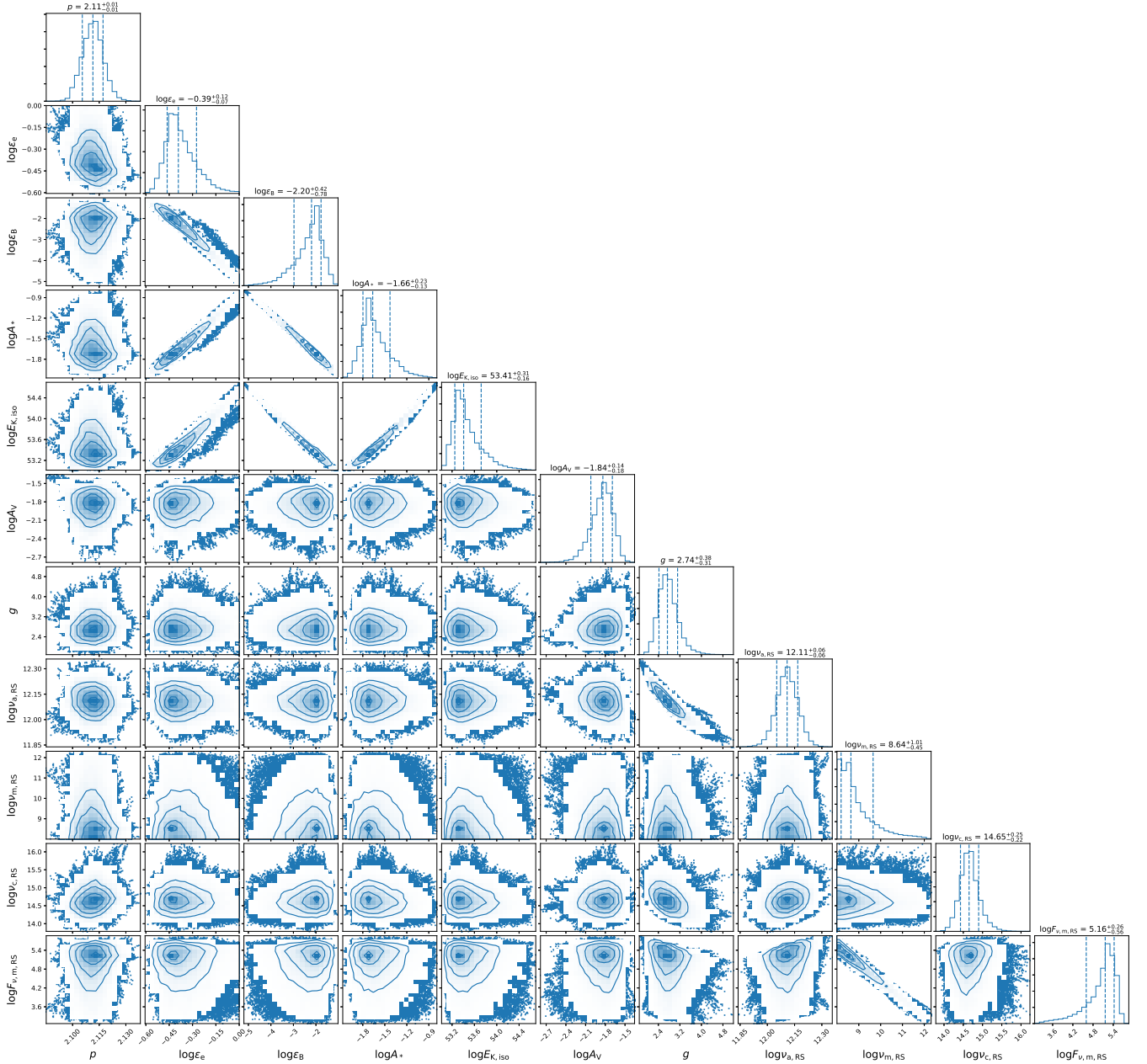
Figure 7. Correlations and marginalized posterior density for all the free parameters in the RS+FS model (not including the host galaxy fluxes). Frequencies are in units of Hz, $F_{\nu,\mathrm{m,r}}$ in mJy, and $E_{\mathrm{K,iso}}$ in erg. The contours enclose 39.3%, 86.4% and 98.9% of the probability mass in each correlation plot (corresponding to 1σ, 2σ, and 3σ regions for two-dimensional Gaussian distributions), while the dashed lines in the histograms indicate the 15.9%, 50% (median), and 84.1% quantiles (corresponding to $\pm 1\sigma$ for one-dimensional Gaussian distributions).

for reference (Figs. 12 and 13).

For this model, the FS cooling frequency, $\nu_{\mathrm{c,f}} \approx 2.6 \times 10^{16}$ Hz at 1 d lies between the optical and X-rays, as expected from the basic considerations in Section 3.2. The proximity of $\nu_{\mathrm{c,f}}$ to the X-ray band ($\nu_{\mathrm{c,f}} \approx 0.3$ keV at 8 days) explains the moderately steep decline in the X-ray light curve, compared to the expectation for $\nu_{\mathrm{X}} \gtrsim \nu_{\mathrm{c,f}}$. Furthermore, $\nu_{\mathrm{a,f}} \approx 60$ MHz is below the VLA and GMRT frequencies, and is therefore not constrained, resulting in degeneracies between the model parameters

(Fig. 7). The FS characteristic frequency at 4 days, $\nu_{\mathrm{m,f}} \approx 6 \times 10^{11}$ Hz is above the ALMA band, as expected from the radio/mm SED at that time (Section 3.1). We list the properties of the best fit model and summarize the marginalized posterior density function in Table 4.

4.2. *Determination of Ejecta Initial Lorentz Factor*

We now use the MCMC results to derive the initial Lorentz factor of the jet. The jet's initial Lorentz factor can be determined from joint RS and FS observations by

solving the following equations self-consistently (Zhang et al. 2003; Laskar et al. 2018c) at the deceleration time, $t_{\rm dec}$,

$$\frac{\nu_{\rm m,r}}{\nu_{\rm m,f}} \sim \Gamma_0^{-2} R_{\rm B},$$

$$\frac{\nu_{\rm c,r}}{\nu_{\rm c,f}} \sim R_{\rm B}^{-3},$$

$$\frac{F_{\nu,\rm m,r}}{F_{\nu,\rm m,f}} \sim \Gamma_0 R_{\rm B}, \qquad (2)$$

where Γ_0 is the initial Lorentz factor of the GRB jet, $R_{\rm B} \equiv (\epsilon_{\rm B,r}/\epsilon_{\rm B,f})^{1/2}$ is the relative magnetization of the ejecta, and we have assumed similar values of $\epsilon_{\rm e}$ and the Compton y parameter in the two regions.

This system of equations has three unknowns ($t_{\rm dec}$, $R_{\rm B}$, and Γ_0), and can be inverted exactly, to yield

$$t_{\rm dec} = t_{\rm ref} \left[\left(\frac{\nu'_{\rm c,f}}{\nu'_{\rm c,r}} \right) \left(\frac{F'_{\nu,\rm m,f}}{F'_{\nu,\rm m,r}} \right)^2 \left(\frac{\nu'_{\rm m,f}}{\nu'_{\rm m,r}} \right) \right]^{\tau},$$

$$\tau \equiv \left[\frac{15}{2(4-k)} - \frac{8(g+3)}{7(2g+1)} \right]^{-1} \qquad (3)$$

where the primed quantities refer to values at the reference time of $t_{\rm ref} = 0.01$ days used in the MCMC analysis. For our best-fit model, this yields $t_{\rm dec} \approx 5.3 \times 10^{-3}$ days or ≈ 460 s; the full MCMC analysis gives $\log(t_{\rm dec}/{\rm days}) = -2.27^{+0.13}_{-0.14}$. We note that this is longer than the burst duration, $T_{90} \approx 172$ s (Section 2), consistent with the thin shell case (Zhang et al. 2003).

Given this value of $t_{\rm dec}$, which satisfies equation 2, we can in principle compute the initial Lorentz factor and magnetization,

$$R_{\rm B} = \left(\frac{\nu_{\rm c,f}}{\nu_{\rm c,r}} \right)^{1/3}$$

$$\Gamma_0 = \frac{F_{\nu,\rm m,r}}{F_{\nu,\rm m,f}} R_{\rm B}^{-1}. \qquad (4)$$

However, we find that whereas $\nu_{\rm c,r}$ and $\nu_{\rm c,f}$ are reasonably well constrained, $F_{\nu,\rm m,r}$ is completely degenerate with $\nu_{\rm m,r}$. This is because the RS peak in the radio band corresponds to $\nu_{\rm a,r}$, and hence the data do not constrain $\nu_{\rm m,r}$. In the observed regime of $\nu_{\rm m,r} < \nu_{\rm a,r}$, the peak flux density of the RS component, $F_{\nu,\rm a,r} \propto F_{\nu,\rm m,r}(\nu_{\rm a,r}/\nu_{\rm m,r})^{(1-p)/2}$ results in the degeneracy, $F_{\nu,\rm m,r} \propto \nu_{\rm m,r}^{(1-p)/2} \propto \nu_{\rm m,r}^{-0.5}$ for $p \approx 2$, which exactly explains the observed correlation between these parameters (Figure 7). Our MCMC samples span 4 orders of magnitude in $\nu_{\rm m,r}$ and correspondingly about 2 orders of magnitude in $F_{\nu,\rm m,r}$. The sampling is clipped at the lower end in $\nu_{\rm m,r}$ by the prior on $\nu_{\rm m,r} > 10^8$ Hz (corresponding to $F_{\nu,\rm m,r} \lesssim 10^8$ mJy) and at the lower end in $F_{\nu,\rm m,r}$ by the actual observed peak flux density of the RS component (corresponding to $\nu_{\rm m,r} \lesssim 10^{12}$ Hz). This degeneracy between $\nu_{\rm m,r}$ and $F_{\nu,\rm m,r}$ does not affect the calculation of $t_{\rm dec}$ (equation 3), because $\nu_{\rm m,r}$ and $F_{\nu,\rm m,r}$ enter in the combination $F_{\nu,\rm m,r}\nu_{\rm m,r}^2 \propto \nu_{\rm m,r}^{2-p}$, which is only weakly dependent on $\nu_{\rm m,r}$ for $p \approx 2$ (i.e., the degenerate terms cancel out). Therefore, we can constrain $t_{\rm dec}$ and $R_{\rm B}$ through this system of equations, but not Γ_0. We find
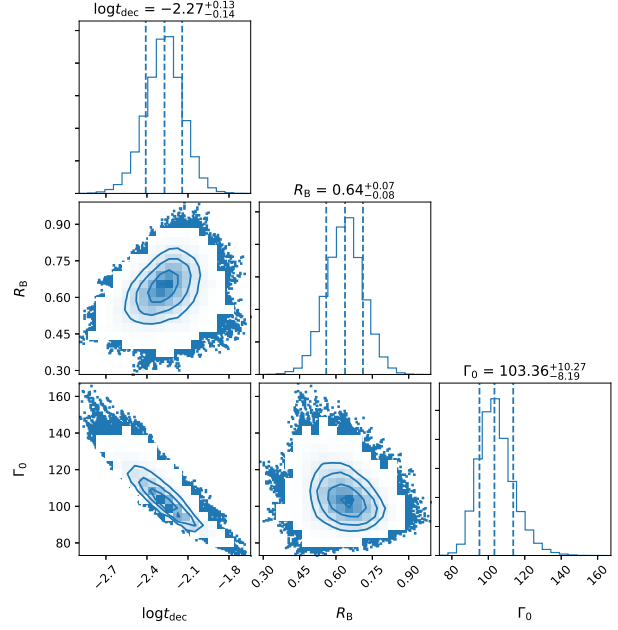

Figure 8. Correlations and marginalized posterior density functions for the deceleration time ($t_{\rm dec}$) and relative magnetization ($R_{\rm B} \equiv (\epsilon_{\rm B,r}/\epsilon_{\rm B,f})^{1/2}$) from the RS-FS consistency argument (equation 4), and the jet initial Lorentz factor (Γ_0), derived using energy balance (equation 8).

$R_{\rm B} \approx 0.65$ for the best-fit solution, and $R_{\rm B} = 0.64^{+0.07}_{-0.08}$ from the MCMC.

To infer Γ_0 in this case, we turn to an energy balance argument (Zhang et al. 2003). At $t_{\rm dec}$, the energy in the swept-up material ($E_{\rm sw}$) is similar to the rest energy of the ejecta (which is the same as the explosion kinetic energy, E),

$$E_{\rm sw} = \Gamma_0^2 M_{\rm sw} c^2 \approx E, \qquad (5)$$

where the swept-up mass at radius, R,

$$M_{\rm sw} = \frac{4\pi A R^{3-k}}{3-k} \qquad (6)$$

Combining equations 5 and 6, the deceleration radius,

$$R = \left[\frac{(3-k)E}{4\pi A \Gamma_0^2 c^2} \right]^{1/(3-k)} = \Gamma_0^{-2/(3-k)} l_{\rm Sedov}, \qquad (7)$$

where $l_{\rm Sedov}$ is the Sedov length, which depends only on the energy and density, parameters that are known from the FS modeling. For a point source moving along the line of sight, this radius corresponds to the deceleration time given by, $R = 2\Gamma_0^2 ct_{\rm dec}/(1+z)$, which gives the initial Lorentz factor,

$$\Gamma_0 \approx \left[\frac{l_{\rm Sedov}}{c} \left(\frac{2t_{\rm dec}}{1+z} \right) \right]^{\frac{3-k}{2(4-k)}} \qquad (8)$$

We note that this is a simplified treatment, and a more rigorous analysis requires integrating over the full fluid profile, and using the specific enthalpy of the shocked region while calculating the swept-up mass. However, for our purposes, this approximate expression will suffice to estimate Γ_0. We compute Γ_0 for all MCMC samples using equation 8, resulting in $\Gamma_0 = 103^{+10}_{-8}$ (Fig. 8).
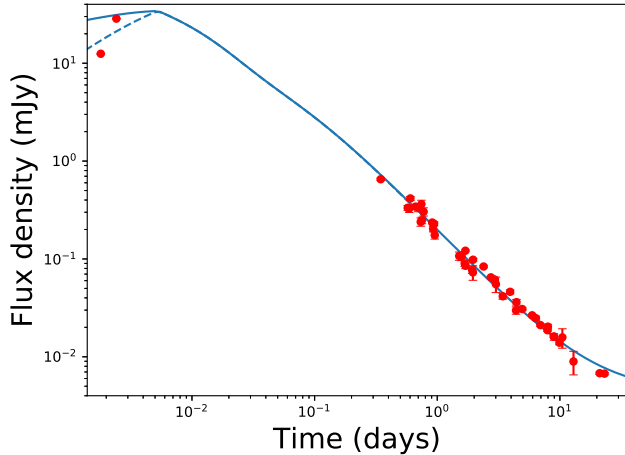
Figure 9. Optical light curve at r'/R and clear band light curve of GRB 181201, together with an FS model with energy injection at $\lesssim t_{\rm dec}$ at the rate expected for a shell at a uniform Lorentz factor, Γ_0, $E \propto t$ (solid) and at an enhanced rate of $E \propto t^{1.8}$ (dashed). The steep optical rise observed with MASTER suggests rapid energy injection into the FS during the deceleration stage (Section 5.1).
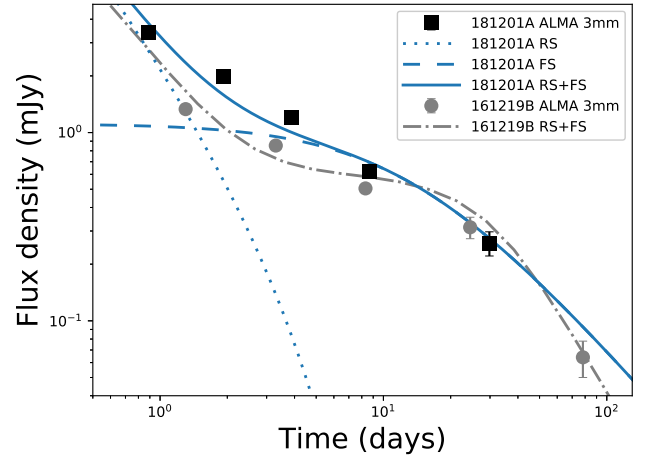

Figure 10. ALMA 3 mm light curve of GRB 181201A (black squares) compared with that of GRB 161219B (grey circles; Laskar et al. 2018c), together with RS+FS models (lines). Both GRBs exhibit excess mm-band emission near the RS-FS transition, indicating additional physics not captured by the model.

5. DISCUSSION

5.1. Early optical rise

We now return to the optical rise observed at $\lesssim 2.4 \times 10^{-3}$ days with MASTER (Fig. 5). These observations were performed at $\lesssim t_{\rm dec}$ in our best-fit RS+FS model (Section 4 and Table 4), consistent with the afterglow onset scenario. The spectral ordering at $t_{\rm dec}$ is $\nu_{\rm m,r} < \nu_{\rm a,r} < \nu_{\rm opt} \approx \nu_{\rm c,r}$ and $\nu_{\rm a,f} < \nu_{\rm c,f} < \nu_{\rm opt} < \nu_{\rm m,f}$. In this model, the RS light curve at $\lesssim t_{\rm dec}$ is expected to rise at the rate $\alpha = (p-1)/2 \approx 0.5$, while the FS light curve should rise as $\alpha = 1/2$ (Zou et al. 2005). However, the observed rise of $\alpha \approx 2.8$ is not consistent with either prediction. The proximity of $\nu_{\rm c,r}$ to $\nu_{\rm opt}$ at the deceleration time may suppress the RS flux. On the other hand, the FS model also over-predicts the observed flux. One possible solution is rapid injection of energy into the FS during this period. We find that an energy increase at the rate $E \propto t^{1.8}$ until $t_{\rm dec}$ roughly accounts for the optical rise[11] (Fig. 9). Such an injection could arise, for instance, by the presence of energy at Lorentz factors $\lesssim \Gamma_0$ owing to velocity stratification in the ejecta (Sari & Mészáros 2000), which has previously been inferred in other GRB afterglows (Laskar et al. 2015; Laskar et al. 2018b,c). An alternate scenario could be a pair-dominated optical flash, as suggested for GRB 130427A (Vurm et al. 2014). However, the paucity of data around the optical peak preclude a more detailed analysis.

5.2. Intermediate millimeter excess

The 3 mm model light curve under-predicts two of the ALMA detections at ≈ 1.9 and ≈ 3.9 days by $\approx 20\%$ (Fig. 10). In particular, the observed light curve exhibits a shallower decline than afforded by the current model, where the transition between RS-dominant to FS-dominant at ≈ 1.5 days results in an inflexion in the

model light curve, which is not seen in the data. One possibility for a shallower RS decline rate is for the RS to be refreshed by slower ejecta catching up with the FS (Sari & Mészáros 2000). This scenario requires a distribution of Lorentz factors in the jet, which has indeed been inferred in other events (Laskar et al. 2015; Laskar et al. 2018b,c), and remains feasible here. We note that a similar discrepancy was present in the only other ALMA light curve of a GRB available at this date, that of GRB 161219B (Laskar et al. 2018c). In that case, the model under-predicts the data at ≈ 3 days, corresponding to a similar RS-FS transition. These similarities may indicate that the RS evolution is more complex than previously thought, or that the mm-band emission is not dominated by the RS at all, and is in fact a separate component. Further ALMA 3 mm observations of GRBs, together with detailed multi-wavelength modeling, may help shed light on this issue.

5.3. Late X-ray excess

The observed 1 keV light curve exhibits a late time shallowing (Fig. 3), and can therefore not be fit perfectly in our model (Fig. 5), where only steepenings are expected (for instance, following a jet break; Sari et al. 1999). As a result, our best-fit model under-predicts the X-ray flux density at 127 days. Above $\nu_{\rm m,f}$, the afterglow light curves are indeed expected to become shallower at late times when the FS becomes non-relativistic at $t_{\rm NR}$ (Waxman et al. 1998). One simple definition of $t_{\rm NR}$ corresponds to the time when $\Gamma\beta \approx 1$ (i.e., $\Gamma \approx \sqrt{2}$). For the best-fit model, these parameters correspond to $t_{\rm NR} \approx 220$ years, which cannot explain the X-ray excess at ≈ 127 days. Another possibility is that the late-time excess corresponds to a contaminating source within the XRT point spread function, which has been observed at least once before; however, this possibility is quite rare and unlikely. One way to test this is to obtain observations of the afterglow with *Chandra*; however, at the time of writing, the target was within an extended Sun-constraint for *Chandra*, and not visible.

We note that late-time excess X-ray flux has been un-

---

[11] The FS dynamics during shock crossing for a shell with a uniform Γ_0 is equivalent to energy injection at the rate $E \propto t$ (Appendix B of Laskar et al. 2015).

covered in other events (Fong et al. 2014; Margutti et al. 2015; Laskar et al. 2018a). Suggested explanations have included dust echoes, inverse-Compton scattering, late-time radiation from spin-down of a magnetar central engine, and interaction of the FS with the shocked stellar wind at the edge of the stellar wind bubble (Shao & Dai 2007; Chandra et al. 2008; Liang et al. 2008; Mimica & Giannios 2011; Gat et al. 2013; Fong et al. 2014; Margutti et al. 2015). For reference, the shock radius at 127 days is ≈ 30 pc for our best-fit parameters, which is significantly larger than the mean distance between O stars in a typical massive stellar cluster (Figer et al. 1999).

5.4. *Late radio excess*

The 1–2 GHz GMRT light curves appear to exhibit an unexpected brightening of the afterglow between 30–48 days after the burst. The corresponding radio maps were dynamic range limited, with noise dominated by image deconvolution errors. Thus, it is possible that our reported uncertainties underestimate the true variation of the non-Gaussian image noise. In that scenario, the light curve may be consistent with being flat, and therefore host-dominated. We caution that while a similar brightening is evident in the GMRT 750 MHz observations, they appear to be absent at 620 MHz. The two bands were observed together as part of a broader frequency coverage with the upgraded GMRT (GWB) system, and no systematic errors are expected in the light curve produced from different parts of the observing band.

On the other hand, we note that late-time light curve flattenings or re-brightenings have been observed in several radio afterglows (Berger et al. 2003a; Panaitescu & Kumar 2004; Alexander et al. 2017; Laskar et al. 2018a,c). If real, the re-brightening in this event might indicate (i) late-time energy injection due to slower ejecta shells[12] (Sari & Mészáros 2000; Kathirgamaraju et al. 2016), which has been inferred in several instances (Laskar et al. 2015; Laskar et al. 2018b,c), or (ii) interaction of the FS with the wind termination shock, a scenario discussed above in the context of the X-ray light curve flattening (Section 5.3). Any contribution from the emerging supernova is expected to peak on $\gtrsim 10$ year time scales, and therefore an unlikely explanation for this excess (Barniol Duran & Giannios 2015). The emergence of a counterjet, such as has been claimed in cm-band observations GRB 980703 at $\gtrsim 500$ days after the burst (Li & Song 2004; Perley et al. 2017) should occur at $\gtrsim t_{\rm NR} \approx 220$ yr for this event (Section 5.3), and is also disfavored.

5.5. *Are we really seeing the reverse shock?*

We note that our derived value of $g \approx 2.7$, while higher than the theoretically expected upper limit for a wind environment (Zou et al. 2005), is comparable to $g \approx 2.3$ in GRB 140304A (Laskar et al. 2015). Previous studies have found even higher values of $g \approx 5$ in the case of the RS emission from GRB 130427A (Laskar et al. 2013; Perley et al. 2014). Higher values of g result in a more slowly evolving spectrum, and are preferred by the fit due to the relatively slowly evolving cm/mm emission observed in these events, including in the event studied here. Owing

to this mismatch with the theoretical prediction for g, as well as some of the other issues described above, it is natural to ask whether the RS+FS model is the only one that can explain the observations. It is possible that the emission observed here and in similar events in the past, which has been ascribed to the RS, is in fact from a different emission mechanism.

One possible alternate explanation is to invoke a two-component jet, one in which the optical and X-ray emission arises from a narrower, faster jet than that producing the cm-band observations (Berger et al. 2003c; Peng et al. 2005; Oates et al. 2007; Racusin et al. 2008; Holland et al. 2012). In such a case, we expect the radio peak frequency and peak flux density to evolve according to the standard FS prescription as $\nu_{\rm m} \propto t^{-3/2}$ and $F_{\nu,{\rm m}} \propto t^{-1/2}$, respectively. From the SED at 3.9 days (Section 3.1 and Fig. 1), this would imply an R-band peak at $\approx 2.2 \times 10^{-3}$ days with a flux density of ≈ 60 mJy. While this would over-predict the MASTER observations at $\approx 2.4 \times 10^{-2}$ days, if the jet producing this emission component were still decelerating at this time, then the flux could be significantly lower. Furthermore, we find that this component would not contribute significantly to the remainder of the optical light curve. For instance, at the time of the earliest UVOT observation at ≈ 0.18 days, the predicted flux density of ≈ 0.2 mJy is below the observed flux density of ≈ 0.6 mJy. Whereas it is not possible for us to confirm or rule out two-component jet models, we note that decoupling the cm/mm emission from the optical/X-ray emission reduces the predictive power of such a model.

Another alternate scenario to explain the radio spectral bump at 3.9 days is the presence of a population of non-accelerated ("thermal") electrons, which are not accelerated by the passage of the FS into a relativistic power-law distribution, but instead form a Maxwellian distribution at lower energies (Eichler & Waxman 2005). However, a disjoint spectral component as observed here would likely require a very specific electron distribution, one in which the typical Lorentz factor of the thermal electrons is much lower than the minimum Lorentz factor of the shock-accelerated electrons, the so-called 'cold electron model' (Ressler & Laskar 2017).

The emission signature from such a population is expected to be quite broad. We demonstrate this by setting the electron participation fraction, usually assumed to be unity, to $f_{\rm NT} \approx 0.6$, and computing the resultant spectrum as described in Ressler & Laskar (2017). We use a cold electron model, with a ratio of electron temperature ($T_{\rm e}$) to gas temperature ($T_{\rm g}$) set at $\eta_{\rm e} \equiv T_{\rm e}/T_{\rm g} \approx 10^{-2}$. The resultant spectrum exhibits a broad peak in the cm-band, and does not match the observations as well as the RS model (Fig. 11). While increasing $f_{\rm NT}$ increases the sharpness of the peak (relative to the underlying FS emission), doing so also increases the relative brightness of the thermal bump beyond the data, and so no combination of $f_{\rm NT}$ and $\eta_{\rm e}$ appears to match the cm-band data. A more detailed analysis requires a complete parameter search over $f_{\rm NT}$ and $\eta_{\rm e}$ that also includes the FS parameters. Such a study is currently not possible due to the computational intensiveness of the thermal electron calculation, and we defer it to future work.

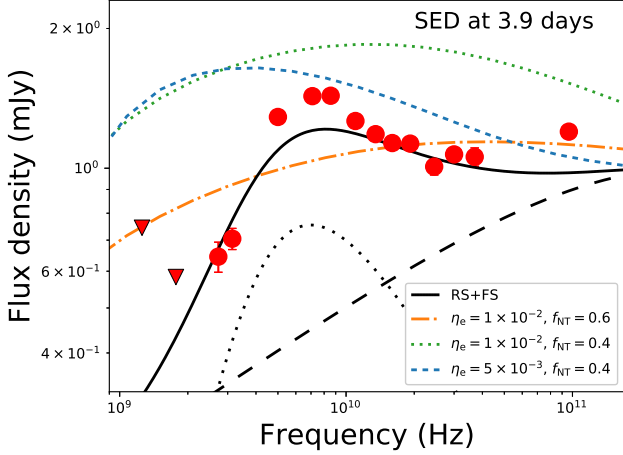[12] the Lorentz factor of the FS is $\Gamma \approx 10$ at 40 days.

Figure 11. SED at 3.9 days (data points), with our best-fit model (solid, black) decomposed into FS (dashed) and RS (dotted) components, compared with a model incorporating thermal electrons (orange dash-dot, blue short dashes, and green dotted). The thermal electron model cannot easily match the sharp spectral peak observed in the cm band.

5.6. FS parameter degeneracies

Our modeling reveals degeneracies between the FS model parameters (Fig. 7), which cannot be explained by the unknown value of $\nu_{a,f}$ alone. For instance, the correlation contours between A_* and $E_{K,iso}$ lie parallel to the degenerate line $E_{K,iso} \propto A_*^{1.4}$. However, the expected relation between these parameters when ν_a is unknown is $E_{K,iso} \propto A_*^{-0.2}$ (Granot & Sari 2002; Laskar et al. 2014). We note that the Compton Y parameter varies by about two orders of magnitude along the axis of the observed degeneracy, and thus the change in the physical parameters is compensated for by varying Y.

Our prescription for calculating Compton Y relies on a simplistic global approximation (Sari & Esin 2001; Laskar et al. 2015). However, we note that in low density environments, the Klein-Nishina suppression limits the maximum value of Y (Nakar et al. 2009). We derive an expression for this maximum value of Y corresponding to the Lorentz factor of cooling electrons in a wind environment by substituting equation (18) from Panaitescu & Kumar (2000) for the effective density as a function of observer time in equation (64) from Nakar et al. (2009) for the maximum value of Y when KN corrections are included, to obtain,

$$Y_{max}(\gamma_c) = 10 e^{\frac{27(3.2-p)^2-17}{(p+2)(4-p)}} e^{\left(\frac{8-p}{2(p+2)} \ln 0.73\right)}$$
$$\times \epsilon_{e,-1}^{\frac{5(p-1)}{p+2}} E_{53}^{\frac{p-3}{p+2}} A_*^{\frac{8-p}{p+2}} t_{days}^{-\frac{(2p-1)}{(p+2)}}. \quad (9)$$

For our best-fit parameters (Table 4), this evaluates to $Y_{max}(\gamma_c) \approx 2 t_{days}^{-0.8}$, which is lower than some of the values in the degenerate models discussed. Thus, a future, more accurate calculation incorporating Klein-Nishina corrections may resolve this source of degeneracy.

5.7. Burst Energetics and radiative efficiency

The data do not reveal a jet break (Rhoads 1999; Sari et al. 1999), and hence the degree of collimation remains unknown for this burst. As of the time of writing, we

are continuing VLA observations of this event, and expect that late-time observations may allow for beaming-independent calorimetry provided the contribution from the underlying host is negligible (Frail et al. 2000; Berger et al. 2003c, 2004; Frail et al. 2005; Shivvers & Berger 2011; De Colle et al. 2012). With that said, we note that our modeling does require some host contribution at 2.7 to 24.5 GHz at the $\approx 50\,\mu$Jy level (Fig. 5), corresponding to a star formation rate of $\approx 2\ M_\odot \mathrm{yr}^{-1}$ (Yun & Carilli 2002; Berger et al. 2003a); hence it is not clear whether such calorimetry will be feasible for this burst. For a jet break time of $t_{jet} \gtrsim 163$ days, we can only set a lower limit to the jet half opening angle of $\theta_{jet} \gtrsim 6°$, corresponding to a minimum beaming-corrected energy of 1.4×10^{52} erg.

The radiative efficiency, on the other hand, is independent of the beaming correction. For our best-fit model, we find $\eta_{rad} \approx 0.35$. This value corresponds to a slightly lower efficiency than for other GRBs at similar $E_{\gamma,iso}$ as derived from X-ray afterglow observations (Lloyd-Ronning & Zhang 2004). However, the observed distribution of η_{rad} for *Swift* GRBs spans a broad range (Berger et al. 2003b; Nousek et al. 2006; Zhang et al. 2007; Beniamini et al. 2015), and this value of η_{rad} is unremarkable.

5.8. Low circum-burst density

There is a strong observed correlation between multi-wavelength detections of RS emission with low density circum-burst environments, typically n_0, $A_* \lesssim 10^{-2}$ (Laskar et al. 2018c). We note that the circum-burst density for our best-fit model, $A_* \approx 0.02$ is also similarly low. We have previously remarked on the possibility that this is an observational selection effect, since low density environments are more likely to result in a slow-cooling RS with long-lasting emission (Laskar et al. 2013, 2016; Laskar et al. 2018c; Laskar et al. 2019; Kopac et al. 2015; Alexander et al. 2017). In the case of GRB 161219B, we used constraints on the RS cooling frequency to determine a maximal particle density for the ISM environment under which RS emission was expected, and showed that the observed density satisfied the constraint in that case. We repeat that argument here, now for the wind medium.

Combining equation 2 with the expression for FS cooling frequency from Granot & Sari (2002),

$$\nu_{c,f} = 4.40 \times 10^{10}(3.45-p)e^{0.45p}(1+z)^{-3/2}$$
$$\times \epsilon_B^{-3/2} A_*^{-2} E_{K,iso,52}^{1/2}(1+Y_f)^{-2} t_d^{1/2}\,\mathrm{Hz}$$
$$\approx 10^{13} A_*^{-2}\,\mathrm{Hz}$$
$$\sim R_B^3 \nu_{c,r} \quad (10)$$

for the best-fit parameters at $t \approx 1$ d yields,

$$A_* \approx \left(\frac{\nu_{c,r}}{10^{13}\,\mathrm{Hz}}\right)^{-1/2} R_B^{-3/2}$$
$$\lesssim 0.24 R_B^{-3/2}\,\mathrm{cm}^{-3}, \quad (11)$$

which is indeed satisfied for GRB 181201A where $A_* \approx 2 \times 10^{-2}$ (corresponding to a mass loss rate, $\dot{M} \approx 2 \times 10^{-7}\ M_\odot \mathrm{yr}^{-1}$ for a wind speed of 10^3 km s^{-1}). We note that a similar low wind parameter of $A_* \approx 3 \times 10^{-3}$ was inferred in the case of GRB 130427A, which also

exhibited a strong RS signature (Laskar et al. 2013; Perley et al. 2014). Our observation of RS emission in GRB 181201A therefore supports the hypothesis that RS emission is more easily detectable in low density environments, in both the ISM and wind scenarios.

5.9. *Reverse shock Lorentz factor*

During our analysis above, we have assumed a non-relativistic reverse shock. We now check this assumption by calculating the Lorentz factor of the RS itself. During the shock crossing, the Lorentz factor of the shocked fluid in the cold ejecta frame is given by

$$\bar{\gamma} \approx \frac{1}{2} \left(\frac{\Gamma_{\rm FS}/\sqrt{2}}{\Gamma_0} + \frac{\Gamma_0}{\Gamma_{\rm FS}/\sqrt{2}} \right), \qquad (12)$$

where $\Gamma_{\rm FS}$ is the FS Lorentz factor, assumed to be highly relativistic. The RS Lorentz factor is then given by the shock jump condition (Blandford & McKee 1976),

$$\bar{\Gamma}_{\rm RS} = \frac{(\bar{\gamma}+1)\left[\hat{\varsigma}\left(\bar{\gamma}-1\right)+1\right]^2}{\hat{\varsigma}(2-\hat{\varsigma})(\bar{\gamma}-1)+2}, \qquad (13)$$

where we take the adiabatic index $\hat{\varsigma} = 4/3$, appropriate for a relativistic fluid (Kobayashi & Sari 2000). We compute these quantities from our MCMC results, and find $\bar{\Gamma}_{\rm RS} = 1.97^{+0.08}_{0.07}$, corresponding to a shock speed of $\bar{\beta}_{\rm RS} = 0.74 \pm 0.02$ and 4-velocity, $\bar{\Gamma}_{\rm RS}\bar{\beta}_{\rm RS} = 1.7 \pm 0.1$. Thus the RS is at most mildly relativistic, and definitely not ultra-relativistic ($\bar{\Gamma}_{\rm RS}\bar{\beta}_{\rm RS} \gg 1$). Whereas the expressions we have used for the RS evolution in the modeling are strictly valid only in the asymptotic regime of a Newtonian RS, they are expected to be approximately correct for cold shells where the post-shock evolution deviates from the Blandford-McKee solution. A more detailed analysis requires numerical calculation of the RS hydrodynamics and radiation simultaneously with the MCMC fitting, which is beyond the scope of this work.

In summary, the detection of the RS signature in this GRB argues against the scenario where the jet is Poynting flux dominated, since in that case, no RS emission is expected (Lyutikov & Camilo Jaramillo 2017). The mildly relativistic RS observed in this case argues against propagation in a highly magnetized, relativistic outflow, such as in a magnetar wind (Metzger et al. 2011). This event brings the number of GRBs with radio RS detections to seven (Kulkarni et al. 1999; Sari & Piran 1999a; Laskar et al. 2013; Perley et al. 2014; Laskar et al. 2016; Alexander et al. 2017; Laskar et al. 2018b,c; Laskar et al. 2019).

5.10. *Ejecta magnetization*

The relative magnetization of $R_{\rm B} \approx 0.6$ observed in this event is similar to $R_{\rm B} \approx 1$ for GRB 161219B (Laskar et al. 2018c) and $R_{\rm B} \approx 0.6$ for GRB 140304A (Laskar et al. 2018b). On the other hand, these values are all smaller than $1 \lesssim R_{\rm B} \lesssim 5$ for GRB 130427A (Laskar et al. 2013), $R_{\rm B} \approx 8$ for GRB 160509A (Laskar et al. 2016), $R_{\rm B} \sim 1$-100 for GRB 160509A (Alexander et al. 2017), and $R_{\rm B} \approx 1$–100 derived for GRBs with optical flashes (Gomboc et al. 2008, 2009; Japelj et al. 2014). Interpreting these values requires accounting for the variation in $\epsilon_{\rm B,f}$ between events, which we perform next.

The plasma magnetization in the ejecta, σ, defined as the ratio of the magnetic energy density to the rest mass energy density, corresponds to $\sigma \approx \epsilon_{\rm B,r}\bar{\Gamma}_{\rm RS}$. For the non-relativistic reverse shocks observed in all of these cases, this implies $\sigma \approx \epsilon_{\rm B,r} = R_{\rm B}^2 \epsilon_{\rm B,f}$. A detailed statistical comparison of σ between GRBs requires full posterior density functions for $R_{\rm B}$ in each case, which are not currently available. However, we can use the typical parameters in each case for a rough comparison. For our best-fit parameters, we have $\epsilon_{\rm B,r} \approx 2.6 \times 10^{-3}$ for GRB 181201A. For GRB 160625B, the large feasible range of $R_{\rm B} \sim 1$–100 makes comparison less meaningful. For GRB 160509A, $R_{\rm B}^2 \epsilon_{\rm B,f} > 1$; however, the RS in that case was long-lived and continuously refreshed, thus suggesting additional physics not captured by the simple calculation of σ. For the other bursts with radio RS emission, we find $\epsilon_{\rm B,r} \approx 6 \times 10^{-2}$ (161219B), $\epsilon_{\rm B,r} \approx 2 \times 10^{-2}$ (140304A), $\epsilon_{\rm B,r} \approx 0.2$–1 (130427A). Thus for all GRBs with detected and well-constrained RS emission, σ ranges between 10^{-3} and ≈ 1, indicating that the ejecta are weakly magnetized. However, we caution that this outcome is largely built into the formalism for non-relativistic reverse shocks, for which $\sigma \approx \epsilon_{\rm B,r}$. The multiwavelength detection and characterization of a relativistic RS might enable us to explore a broader regime in σ.

6. CONCLUSIONS

We have presented multi-wavelength radio to X-ray observations of GRB 181201A spanning from ≈ 150 s to ≈ 163 days after the burst. We have modeled these observations in the standard afterglow synchrotron emission framework to derive the burst energetics and parameters of the explosion. The radio data we present reveal the presence of an additional component, which we interpret as emission from electrons heated by a mildly relativistic ($\bar{\Gamma}_{\rm RS} \approx 2$) reverse shock that propagates through the ejecta in $t_{\rm dec} \approx 460$ s. We have performed detailed, self-consistent modeling of the RS and FS to derive the initial Lorentz factor, $\Gamma = 103^{+10}_{-8}$ and magnetization, $R_{\rm B} \equiv B_{\rm RS}/B_{\rm FS} = 0.64^{+0.07}_{-0.08}$ of the jet that produced this gamma-ray burst. The low inferred ejecta magnetization disfavors a Poynting flux-dominated outflow. The derived low circum-burst density is consistent with the emerging requirement of low density environments for long-lasting, detectable RS emission to be produced. The MCMC analysis performed here explores degeneracies between the RS and FS parameters for the first time, and can be used to derive the properties of the ejecta and surrounding environment. Our results reveal additional degeneracies in the forward shock parameters due to an incomplete treatment of inverse Compton cooling; future work that incorporates the Klein-Nishina corrections may help alleviate this problem, allowing for even better constraints on the underlying physical processes and central engine responsible for GRBs and their afterglows.

public of Korea), in cooperation with the Republic of Chile. The Joint ALMA Observatory is operated by ESO, AUI/NRAO and NAOJ. VLA observations for this study were obtained via project 18A-088 and 18B-407 (PI: Laskar). The National Radio Astronomy Observatory is a facility of the National Science Foundation operated under cooperative agreement by Associated Universities, Inc. GMRT observations for this study were obtained via project 35_065 (PI: Laskar). We thank the staff of the GMRT that made these observations possible. GMRT is run by the National Centre for Radio Astrophysics of the Tata Institute of Fundamental Research. MASTER equipment is supported by the Development Program of Lomonosov MSU and by Moscow Union Optika. MASTER-SAAO is supported by National Research Foundation of South Africa. We thank J. Rupert for obtaining some of the MDM observations. This work is based in part on observations obtained at the MDM Observatory, operated by Dartmouth College, Columbia University, Ohio State University, Ohio University, and the University of Michigan. The Bath Astrophysics Group acknowledges support from the University of Bath and the Science and Technologies Facilities Council. KDA acknowledges support provided by NASA through the NASA Hubble Fellowship grant HST-HF2-51403.001 awarded by the Space Telescope Science Institute, which is operated by the Association of Universities for Research in Astronomy, Inc., for NASA, under contract NAS5-26555. RBD acknowledges support from the National Science Foundation under Grant 1816694. The Berger Time-Domain Group at Harvard is supported in part by NSF under grant AST-1714498 and by NASA under grant NNX15AE50G. RC thanks the Kavli Institute for Theoretical Physics for its hospitality while some of this work was completed. This research was supported in part by the National Science Foundation under Grant No. NSF PHY-1748958. AG acknowledges the financial support from the Slovenian Research Agency (grants P1-0031, I0-0033, and J1-8136) and networking support by the COST Actions CA16104 GWverse and CA16214 PHAROS. NJ is supported by a Jim and Hiroko Sherwin Studentship in Astrophysics. VL, EG, and NT acknowledge support by the Russian Foundation for Basic Research 17-52-8013. RY is in part supported by Grants-in-Aid for KAKENHI grants No. 18H01232. This work makes use of data supplied by the UK Swift Science Data Centre at the University of Leicester and of data obtained through the High Energy Astrophysics Science Archive Research Center On-line Service, provided by the NASA/Goddard Space Flight Center.

Figure 12. Multi-band SEDs of GRB 181201A from ≈ 0.9 to ≈ 163.4 days, together with the FS+RS model presented in Section 4. The combined model explains the overall behavior of the afterglow spanning over 8 orders of magnitude in frequency and over 2 orders of magnitude in time.

REFERENCES

Akerlof, C., Balsano, R., Barthelmy, S., et al. 1999, Nature, 398, 400
Alexander, K. D., Laskar, T., Berger, E., et al. 2017, ApJ, 848, 69
Amati, L. 2006, MNRAS, 372, 233
Arimoto, M., Axelsson, M., & Ohno, M. 2018, GRB Coordinates Network, Circular Service, No. 23480, #1 (2018/December-0), 23480
Barniol Duran, R., & Giannios, D. 2015, MNRAS, 454, 1711
Beniamini, P., Nava, L., Duran, R. B., & Piran, T. 2015, MNRAS, 454, 1073
Berger, E., Cowie, L. L., Kulkarni, S. R., et al. 2003a, ApJ, 588, 99
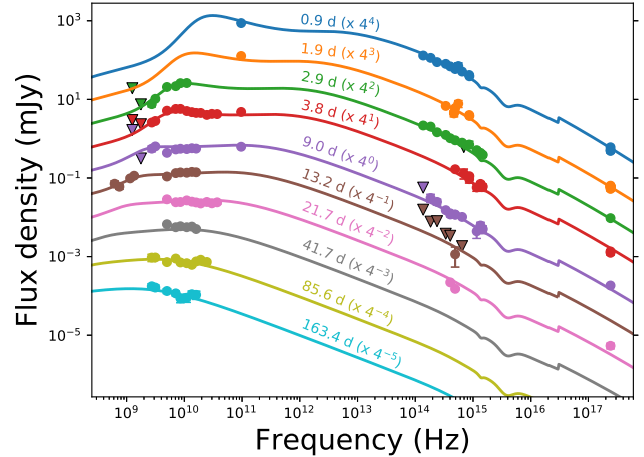Berger, E., Kulkarni, S. R., & Frail, D. A. 2003b, ApJ, 590, 379
—. 2004, ApJ, 612, 966
Berger, E., Kulkarni, S. R., Pooley, G., et al. 2003c, Nature, 426, 154
Blandford, R. D., & McKee, C. F. 1976, Physics of Fluids, 19, 1130
Bradley, L., Sipocz, B., Robitaille, T., et al. 2016, Photutils: Photometry tools, ascl:1609.011
Burrows, D. N., Hill, J. E., Nousek, J. A., et al. 2005, Space Sci. Rev., 120, 165
Chandra, P., Cenko, S. B., Frail, D. A., et al. 2008, ApJ, 683, 924
Chevalier, R. A., & Li, Z.-Y. 2000, ApJ, 536, 195
De Colle, F., Ramirez-Ruiz, E., Granot, J., & Lopez-Camara, D. 2012, ApJ, 751, 57
Eichler, D., & Waxman, E. 2005, ApJ, 627, 861
Figer, D. F., McLean, I. S., & Morris, M. 1999, ApJ, 514, 202
Fong, W., Berger, E., Metzger, B. D., et al. 2014, ApJ, 780, 118
Foreman-Mackey, D., Hogg, D. W., Lang, D., & Goodman, J. 2013, PASP, 125, 306
Frail, D. A., Kulkarni, S. R., Nicastro, L., Feroci, M., & Taylor, G. B. 1997, Nature, 389, 261
Frail, D. A., Soderberg, A. M., Kulkarni, S. R., et al. 2005, ApJ, 619, 994
Frail, D. A., Waxman, E., & Kulkarni, S. R. 2000, ApJ, 537, 191
Gat, I., van Eerten, H., & MacFadyen, A. 2013, ApJ, 773, 2
Gomboc, A., Kobayashi, S., Guidorzi, C., et al. 2008, ApJ, 687, 443
Gomboc, A., Kobayashi, S., Mundell, C. G., et al. 2009, in American Institute of Physics Conference Series, Vol. 1133, American Institute of Physics Conference Series, ed. . N. G. C. Meegan, C. Kouveliotou, 145–150
Granot, J., & Königl, A. 2003, ApJ, 594, L83
Granot, J., & Sari, R. 2002, ApJ, 568, 820
Granot, J., & Taylor, G. B. 2005, ApJ, 625, 263
Holland, S. T., De Pasquale, M., Mao, J., et al. 2012, ApJ, 745, 41
Izzo, L., de Ugarte Postigo, A., Kann, D. A., et al. 2018, GRB Coordinates Network, Circular Service, No. 23488, #1 (2018/December-0), 23488
Japelj, J., Kopač, D., Kobayashi, S., et al. 2014, ApJ, 785, 84
Kathirgamaraju, A., Barniol Duran, R., & Giannios, D. 2016, MNRAS, 461, 1568
Khanam, T., Sharma, V., Vibhute, A., et al. 2018, GRB Coordinates Network, Circular Service, No. 23501, #1 (2018/December-0), 23501
Kobayashi, S. 2000, ApJ, 545, 807
Kobayashi, S., Piran, T., & Sari, R. 1999, ApJ, 513, 669
Kobayashi, S., & Sari, R. 2000, ApJ, 542, 819
Kobayashi, S., & Zhang, B. 2007, ApJ, 655, 973
Kong, A. K. H. 2018, GRB Coordinates Network, Circular Service, No. 23475, #1 (2018/December-0), 23475
Kopac, D., Mundell, C. G., Kobayashi, S., et al. 2015, ApJ, 806, 179
Krühler, T., Küpcü Yoldaş, A., Greiner, J., et al. 2008, ApJ, 685, 376
Kulkarni, S. R., Frail, D. A., Sari, R., et al. 1999, ApJ, 522, L97
Laskar, T., Berger, E., Chornock, R., et al. 2018a, ApJ, 858, 65
Laskar, T., Berger, E., Margutti, R., et al. 2015, ApJ, 814, 1
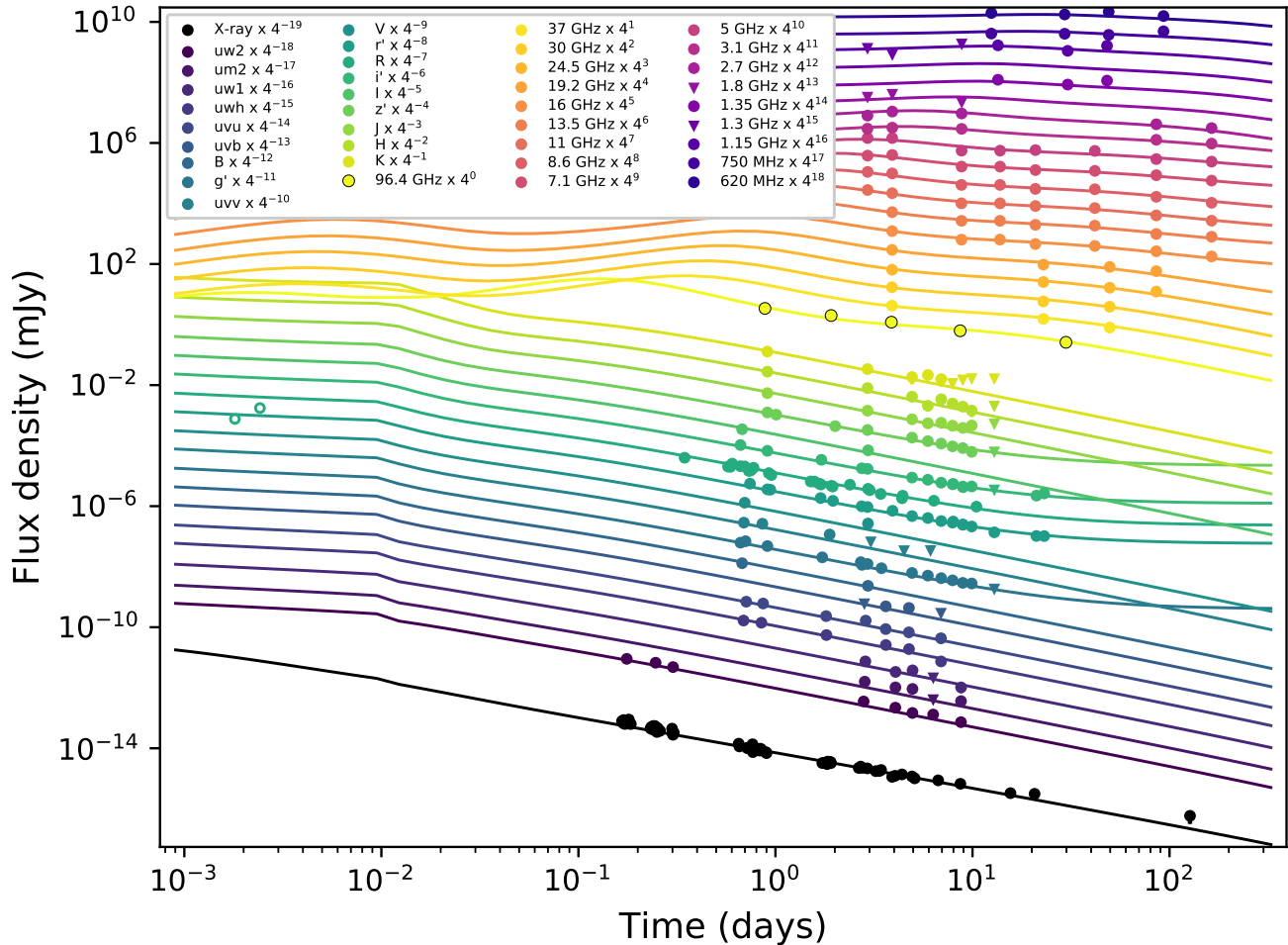Laskar, T., Berger, E., Zauderer, B. A., et al. 2013, ApJ, 776, 119

Figure 13. X-ray to radio light curves of GRB 181201A, together with the FS+RS model presented in Section 4, presented together for reference. The combined model explains the overall behavior of the light curves at all 36 observing frequencies.

Laskar, T., Berger, E., Tanvir, N., et al. 2014, ApJ, 781, 1
Laskar, T., Alexander, K. D., Berger, E., et al. 2016, ApJ, 833, 88
Laskar, T., Berger, E., Margutti, R., et al. 2018b, ApJ, 859, 134
Laskar, T., Alexander, K. D., Berger, E., et al. 2018c, ApJ, 862, 94
Laskar, T., Alexander, K. D., Gill, R., et al. 2019, ApJL, 878, L26
Li, Z., & Song, L. M. 2004, ApJ, 614, L17
Liang, E.-W., Racusin, J. L., Zhang, B., Zhang, B.-B., & Burrows, D. N. 2008, ApJ, 675, 528
Liang, E.-W., Yi, S.-X., Zhang, J., et al. 2010, ApJ, 725, 2209
Lipunov, V., Kornilov, V., Gorbovskoy, E., et al. 2010, Advances in Astronomy, 2010, 349171
Lipunov, V. M., Vladimirov, V. V., Gorbovskoi, E. S., et al. 2019, Astronomy Reports, 63, 293
Lloyd-Ronning, N. M., & Zhang, B. 2004, ApJ, 613, 477
Lyutikov, M., & Camilo Jaramillo, J. 2017, ApJ, 835, 206
Margutti, R., Guidorzi, C., Lazzati, D., et al. 2015, ApJ, 805, 159
Martini, P., Stoll, R., Derwent, M. A., et al. 2011, PASP, 123, 187
McMahon, E., Kumar, P., & Piran, T. 2006, MNRAS, 366, 575
McMullin, J. P., Waters, B., Schiebel, D., Young, W., & Golap, K. 2007, in Astronomical Society of the Pacific Conference Series, Vol. 376, Astronomical Data Analysis Software and Systems XVI, ed. R. A. Shaw, F. Hill, & D. J. Bell, 127
Melandri, A., Kobayashi, S., Mundell, C. G., et al. 2010, ApJ, 723, 1331
Mereghetti, S., Gotz, D., Ferrigno, C., et al. 2018, GRB Coordinates Network, Circular Service, No. 23469, #1 (2018/December-0), 23469
Mészáros, P. 2006, Reports on Progress in Physics, 69, 2259
Meszaros, P., & Rees, M. J. 1993, ApJ, 405, 278
Mészáros, P., & Rees, M. J. 1999, MNRAS, 306, L39
Metzger, B. D., Giannios, D., Thompson, T. A., Bucciantini, N., & Quataert, E. 2011, MNRAS, 413, 2031

Mimica, P., & Giannios, D. 2011, MNRAS, 418, 583
Molinari, E., Vergani, S. D., Malesani, D., et al. 2007, A&A, 469, L13
Nakar, E., Ando, S., & Sari, R. 2009, ApJ, 703, 675
Nakar, E., & Piran, T. 2004, MNRAS, 353, 647
Nousek, J. A., Kouveliotou, C., Grupe, D., et al. 2006, ApJ, 642, 389
Oates, S. R., de Pasquale, M., Page, M. J., et al. 2007, MNRAS, 380, 270
Panaitescu, A., & Kumar, P. 2000, ApJ, 543, 66
Panaitescu, A., & Kumar, P. 2004, MNRAS, 350, 213
Peng, F., Königl, A., & Granot, J. 2005, ApJ, 626, 966
Perley, D. A., Hjorth, J., Tanvir, N. R., & Perley, R. A. 2017, MNRAS, 465, 970
Perley, D. A., Cenko, S. B., Corsi, A., et al. 2014, ApJ, 781, 37
Podesta, R., Lopez, C., Podesta, F., et al. 2018, GRB Coordinates Network, Circular Service, No. 23470, #1 (2018/December-0), 23470
Poole, T. S., Breeveld, A. A., Page, M. J., et al. 2008, MNRAS, 383, 627
Racusin, J. L., Karpov, S. V., Sokolowski, M., et al. 2008, Nature, 455, 183
Rees, M. J., & Meszaros, P. 1992, MNRAS, 258, 41P
—. 1994, ApJ, 430, L93
Ressler, S. M., & Laskar, T. 2017, ApJ, 845, 150
Rhoads, J. E. 1999, ApJ, 525, 737
Roming, P. W. A., Kennedy, T. E., Mason, K. O., et al. 2005, Space Sci. Rev., 120, 95
Sari, R., & Esin, A. A. 2001, ApJ, 548, 787
Sari, R., & Mészáros, P. 2000, ApJ, 535, L33
Sari, R., & Piran, T. 1999a, ApJ, 517, L109
—. 1999b, ApJ, 520, 641
Sari, R., Piran, T., & Halpern, J. P. 1999, ApJ, 519, L17

Sari, R., Piran, T., & Narayan, R. 1998, ApJ, 497, L17+
Schlafly, E. F., & Finkbeiner, D. P. 2011, ApJ, 737, 103
Shao, L., & Dai, Z. G. 2007, ApJ, 660, 1319
Shivvers, I., & Berger, E. 2011, ApJ, 734, 58
Siegel, M. H., & Cannizzo, J. K. 2018, GRB Coordinates Network,
    Circular Service, No. 23499, #1 (2018/December-0), 23499
Steele, I. A., Smith, R. J., Rees, P. C., et al. 2004, in Proc. SPIE,
    Vol. 5489, Ground-based Telescopes, ed. J. M. Oschmann, Jr.,
    679–692
Svinkin, D., Golenetskii, S., Aptekar, R., et al. 2018, GRB
    Coordinates Network, Circular Service, No. 23495, #1
    (2018/December-0), 23495
Troja, E., Lipunov, V. M., Mundell, C. G., et al. 2017, Nature,
    547, 425

van der Horst, A. J., Paragi, Z., de Bruyn, A. G., et al. 2014,
    MNRAS, 444, 3151
Vurm, I., Hascoët, R., & Beloborodov, A. M. 2014, ApJ, 789, L37
Waxman, E., Kulkarni, S. R., & Frail, D. A. 1998, ApJ, 497, 288
Woosley, S. E., & Bloom, J. S. 2006, ARA&A, 44, 507
Yun, M. S., & Carilli, C. L. 2002, ApJ, 568, 88
Zhang, B., & Kobayashi, S. 2005, ApJ, 628, 315
Zhang, B., Kobayashi, S., & Mészáros, P. 2003, ApJ, 595, 950
Zhang, B., Liang, E., Page, K. L., et al. 2007, ApJ, 655, 989
Zou, Y. C., Wu, X. F., & Dai, Z. G. 2005, MNRAS, 363, 93